



Scatter Analysis along the Multidimensional Radius–Luminosity Relations for Reverberation-mapped Mg II Sources

Mary Loli Martínez–Aldama¹ , Michal Zajaček¹ , Bożena Czerny¹ , and Swayamtrupta Panda^{1,2}

¹Center for Theoretical Physics, Polish Academy of Sciences, Al. Lotników 32/46, 02-668 Warsaw, Poland; mmary@cft.edu.pl

²Nicolaus Copernicus Astronomical Center, Polish Academy of Sciences, ul. Bartycka 18, 00-716 Warsaw, Poland

Received 2020 July 18; revised 2020 September 7; accepted 2020 September 8; published 2020 November 4

Abstract

The usage of the radius–luminosity (R – L) relation for the determination of black hole masses across the cosmic history, as well as its application for cosmological studies, motivates us to analyze its scatter, which has recently increased significantly for both the optical ($H\beta$) and UV (Mg II) lines. To this purpose, we determined the scatter along the R – L relation for an up-to-date reverberation-mapped Mg II sample. Studying linear combinations of the luminosity at 3000 Å with independent parameters such as the FWHM, the UV Fe II strength ($R_{\text{Fe II}}$), and the fractional variability (F_{var}) for the whole sample, we get only a small decrease in the scatter ($\sigma_{\text{rms}} = 0.29 - 0.30$ dex). Linear combinations with the dimensionless accretion rate (\dot{M}) and the Eddington ratio lead to significant reductions of the scatter ($\sigma_{\text{rms}} \sim 0.1$ dex), albeit both suffering from the interdependency on the observed time delay. After the division into two subsamples considering the median value of the \dot{M} in the full sample, we find that the scatter decreases significantly for the highly accreting subsample. In particular, the smallest scatter of $\sigma_{\text{rms}} = 0.17$ dex is associated with the independent parameter $R_{\text{Fe II}}$, followed by the combination with F_{var} with $\sigma_{\text{rms}} = 0.19$ dex. Both of these independent observationally inferred parameters are in turn correlated with \dot{M} and $L_{\text{bol}}/L_{\text{Edd}}$. These results suggest that the large scatter along the R – L relation is driven mainly by the accretion rate intensity.

Unified Astronomy Thesaurus concepts: Active galaxies (17); Supermassive black holes (1663)

Supporting material: machine-readable table

1. Introduction

Strong and broad emission lines are among the most characteristic features of the type 1 active galactic nuclei (AGNs; for a review, see Netzer 2013). The broad-line region (BLR) where these lines originate was only recently marginally resolved in 3C 273 with the near-infrared interferometry instrument GRAVITY (Gravity Collaboration et al. 2018), but in all other objects the access to the BLR structure is only through variability studies. The reverberation mapping (RM) technique—the observation of the response of the BLR lines to the changing continuum (Blandford & McKee 1982; Peterson & Horne 2004; Gaskell 2009; Czerny 2019)—has been applied now to over 100 objects, mostly using $H\beta$ lines but also for several other lines (see, e.g., Netzer 2020, and the references therein).

The major discovery coming from this research field was the radius–luminosity (R – L) relation between the time delay of the $H\beta$ line and the continuum luminosity measured at 5100 Å (Kaspi et al. 2000; Peterson et al. 2004; Bentz et al. 2013). Assuming that the line-emitting clouds are virialized, the R – L relation, with a relatively small scatter of 0.19 dex (only 0.13 dex with one source removed; see Bentz et al. 2013), allowed for massive inference of black hole masses in AGNs using just single-epoch spectra, with the line width (FWHM, or σ_{line} -line dispersion) serving as a proxy for the BLR velocity (e.g., Peterson et al. 2004; Collin et al. 2006; Vestergaard & Peterson 2006; Denney et al. 2013; Mejía-Restrepo et al. 2018; Dalla Bontà et al. 2020; Yu et al. 2020a), and the monochromatic luminosity serving as a proxy for the BLR radius. It also started to be considered as a promising tool for measuring luminosity distances in cosmology, making AGNs standardizable candles, as the time delay of the BLR lines

could be used as a proxy for a redshift-independent measurement of the absolute luminosity (Haas et al. 2011; Watson et al. 2011; Czerny et al. 2013; Martínez-Aldama et al. 2019; Panda et al. 2019a). The small scatter in the R – L relation is potentially explained by the failed radiatively accelerated dusty outflow (FRADO), a theoretical model of the BLR that connected the inner radius of the BLR to the monochromatic flux through the request of the disk surface temperature to be equal to the dust sublimation temperature (Czerny & Hryniewicz 2011; Czerny et al. 2017).

Reverberation mapping requires high-cadence, long-duration monitoring. Since it is very difficult to get a large number of time-critical observations on oversubscribed facilities for a technique that is still under development, early reverberation mapping programs were carried out on smaller telescopes, which in turn restricted observations to apparently bright, relatively nearby AGNs, especially those already known to have variable broad emission lines. Furthermore, many reverberation programs used the [O III] $\lambda\lambda 5007, 4959$ narrow lines as an internal flux calibrator because they arise in a more extended, lower-density environment and are expected to be constant in flux over reverberation timescales (Peterson et al. 1998a). These considerations conspired to bias the early reverberation samples toward lower Eddington ratio sources. With a growing interest in the behavior of different types of AGNs (e.g., supermassive black holes with high accretion rates; Du et al. 2014, 2018), and with the start of Sloan Digital Sky Survey Reverberation Mapping Project (SDSS-RM) based on selection of a part of the sky instead of individual sources, the scatter in the R – L has increased considerably. The scatter was seen both in $H\beta$ studies (Grier et al. 2017) and in most recent studies based on the Mg II line (Czerny et al. 2019a;

Homayouni et al. 2020; Zajaček et al. 2020). This poses two fundamental questions: (1) What is the physical cause of this dispersion? (2) Is there a way to still use the R – L relation reliably for black hole mass estimates, as well as for the cosmology?

The scatter is apparently related to the accretion rate intensities, where the sources with the largest accretion rate show the largest departures from the R – L relation (e.g., Du et al. 2018), which increases its overall scatter. In order to take into account the accretion rate effect, a correction based on the dimensionless accretion rate parameter, as well as the Eddington ratio, was proposed by Martínez-Aldama et al. (2019) and Dalla Bontà et al. (2020). However, the interdependence between these parameters and the observed time delay (τ_{obs}) makes it less reliable (Fonseca Alvarez et al. 2020). Since a few independent observationally inferred parameters are driven by the accretion rate intensity, they can also be considered to recover the low scatter. For instance, the optical Fe II strength is related to the accretion rate intensity; then, including this parameter in the R – L relation, the scatter decreases significantly ($\sigma \sim 0.19$ dex; Du & Wang 2019; Yu et al. 2020b).

In the present paper we analyze the multidimensional view of the R – L relation using the measurements of the Mg II time delay. The sample used is relatively homogeneous, coming from a small number of research groups (Section 2). We analyze how the scatter changes when the observed time delay is expressed as a linear combination of the logarithms of relevant quantities, including the monochromatic luminosity at 3000 Å, the FWHM, the interdependent accretion rate parameters (dimensionless \dot{M} and the Eddington ratio, $L_{\text{bol}}/L_{\text{Edd}}$), and other parameters correlated with the accretion rate, such as the strength of the UV Fe II line ($R_{\text{Fe II}}$) and the fractional variability, F_{var} (Section 3). We discuss certain relevant issues in Section 4 and summarize our results in Section 5.

2. Sample and Measurements

2.1. Sample Description

The full sample includes 68 objects with $42.8 < \log L_{3000} < 46.8$ at $0.003 < z < 1.89$. It includes all the objects with reverberation-mapped Mg II measurements reported to date. The sample includes the 57 Mg II time lags (henceforth SDSS-RM sample) from the recent SDSS-RM monitoring (Homayouni et al. 2020) and the six objects previously monitored by the same project (Shen et al. 2016). Only one object from the previous SDSS-RM monitoring is included in the recent one; both measurements are considered. We also include the high-luminosity objects: CTS 252 monitored by Lira et al. (2018), CTS C30.10 measured by Czerny et al. (2019a), HE 0413-4031 monitored by Zajaček et al. (2020), and the two old *IUE* measurements reported for NGC 4151 by Metzroth et al. (2006).

The full sample considered is relatively homogeneous, since $\sim 83\%$ of the objects come from the SDSS-RM sample and $\sim 9\%$ from their previous program. The rest of the objects with the lowest (NGC 4151) and the highest (CTS C30.10, HE 0413-4031, and CTS 252) luminosities are crucial for the detection of the trends in the R – L relation. For the recent SDSS-RM sample, the time delay is estimated using the JAVELIN method (Zu et al. 2011, 2013, 2016), while for the rest of the sources other methods are applied, specifically the interpolated cross-correlation function (ICCF; Gaskell &

Peterson 1987; Peterson et al. 1998b), the discrete correlation function (DCF; Edelson & Krolik 1988), the z -transformed DCF (zDCF; Alexander 1997), the light-curve similarity estimators (Von Neumann or Bartels estimators; Chelouche et al. 2017), and the χ^2 method (Czerny et al. 2013, 2019a; Zajaček et al. 2020), or an average of them. Recent statistical analyses (Li et al. 2019; Yu et al. 2020) point out that the JAVELIN method is more powerful than other traditional methods (ICCF and zDCF) to recover time delays. However, the analyses were performed on the mock sample where the continuum light curve is generated using the damped random-walk (DRW) process, and the JAVELIN method makes use of the DRW to recover the time delay. Therefore, there may be a bias since the stochastic, red-noise part of the variable continuum is omitted in the generated light curves from their power-density spectra. In particular, the model-independent, discrete methods such as zDCF and the von Neumann estimator may still be more suitable for the analysis of irregular and heterogeneous light curves of more distant quasars (Czerny et al. 2019a; Zajaček et al. 2019, 2020). In particular, for the highly accreting source HE 0413-4031 at $z = 1.39$, Zajaček et al. (2020) saw a difference between JAVELIN and ICCF on one hand and discrete methods (DCF, zDCF, and von Neumann) on the other hand, in the determination of the primary time delay peak, $\tau \sim 431$ and ~ 303 days, respectively.

In addition, each research group assumes different time delay significance criteria, which may not be satisfied for the objects of other samples. For example, the recent SDSS-RM monitoring (Homayouni et al. 2020) considers that a time delay is statistically significant if (1) a primary time-lag peak includes at least 60% of the weighted time delay posterior samples and (2) the time delay is well detected at the 3σ level different from the zero time delay. Therefore, for completeness, we consider all the objects as we analyze a mixed sample, for which it is difficult to establish general statistically robust criteria.

2.2. Measurements

For all the sources in the sample, we collected several measured parameters, which are summarized in Table B1 in Appendix B. For the SDSS-RM sample, the luminosity at 3000 Å, FWHM, and equivalent width (EW) of Mg II and Fe II (at 2250–2650 Å) were taken from the Shen et al. (2019) catalog, which assumes a flat Λ CDM cosmology with $\Omega_{\Lambda} = 0.7$ and $H_0 = 70 \text{ km s}^{-1} \text{ Mpc}^{-1}$. The time delay is taken from Homayouni et al. 2020. They estimated time delays of Mg II by two methods: JAVELIN and CREAM. In this contribution we use the JAVELIN estimations since they are more reliable according to the authors. For the rest of the sample, the measurements were taken from the compilation done by Zajaček et al. (2020, see their Table 2).

Since in the optical range the strength of the Fe II broad line shows a clear correlation with the accretion rate intensity (Boroson 2002; Negrete et al. 2018; Du & Wang 2019; Panda et al. 2019b), we explore a similar correlation considering the UV Fe II. The relation between the UV Fe II and the accretion parameters is scarcely studied (Dong et al. 2011), but since the UV and optical Fe II are correlated, and in turn both show similar anticorrelations with the FWHM of H β (Dong et al. 2009, 2011; Kovačević-Dojčinović & Popović 2015; Śniegowska et al. 2020), it opens the possibility that the UV Fe II is also related to the accretion rate intensity as is the

optical Fe II emission. In Appendix A, we include a discussion about this issue considering the parameters estimated below.

The UV Fe II strength is estimated using the parameter $R_{\text{Fe II}}$, which is defined as the ratio of the equivalent width of Fe II pseudo-continuum measured at 2250–2650 Å to the EW of the Mg II line:

$$R_{\text{Fe II}} = \frac{\text{EW (UV Fe II)}}{\text{EW (Mg II)}}. \quad (1)$$

The wavelength range selected for the EW of UV Fe II is defined by the one reported in the Shen et al. (2019) catalog. In the case of quasars CTS C30.10 and HE 0413-4031, UV Fe II was directly measured only in the 2700–2900 Å range and for a different UV Fe II template, but for consistency we refitted these spectra using the UV Fe II template of Vestergaard & Wilkes (2001) and rescaled the newly derived EW(Fe II) from 2700–2900 Å to 2250–2650 Å by the factor of 2.32 appropriate for the Vestergaard & Wilkes (2001) UV Fe II template. For NGC 4151 and CTS 252, the EW of Mg II and UV Fe II is not reported in the required wavelength range, and hence we do not consider these objects in the analysis where $R_{\text{Fe II}}$ is used.

We also estimated the level of variability using the F_{var} parameter (Rodríguez-Pascual et al. 1997), defined by

$$F_{\text{var}} = \frac{(\sigma^2 - \Delta)^{1/2}}{\langle f \rangle}, \quad (2)$$

where σ^2 is the variance of the flux, Δ is the mean square value of the uncertainties (Δ_i) associated with each flux measurement (f_i), and $\langle f \rangle$ is the mean flux. F_{var} or similar expressions of the variability level are also correlated with the accretion rate intensity (Wilhite et al. 2005; MacLeod et al. 2010; Sánchez-Sáez et al. 2018; Martínez-Aldama et al. 2019). For the SDSS-RM sample, we use the fractional rms variability provided by the Shen et al. (2019) catalog (see their Table 2) for estimating F_{var} , while the F_{var} values for the rest of the objects were taken from their originals works.

Furthermore, we consider the secondary parameters that can be derived from the basic measurements and in turn from the black hole mass: the dimensionless accretion rate (\dot{M}) and the Eddington ratio ($L_{\text{bol}}/L_{\text{Edd}}$). Several results indicate that line dispersion (σ_{line}) is a better estimator of the velocity field and in turn a better entity for the estimation of the black hole mass, because it is less biased than the FWHM (e.g., Peterson et al. 2004; Denney et al. 2013; Dalla Bontà et al. 2020; Yu et al. 2020a). However, since σ_{line} is not reported for the SDSS-RM sample, which includes the majority of the sources used in this paper, our estimations are done considering the FWHM taken from the Shen et al. (2019) catalog. Then, to get the black hole mass (M_{BH}) estimation, we consider a virial factor anticorrelated with the FWHM of the emission line defined as $f_c = (\text{FWHM}_{\text{Mg II}}/3200 \pm 800)^{-1.21 \pm 0.24}$ (Mejía-Restrepo et al. 2018), the time delay (τ_{obs}) of Mg II reported in Table B1 (Appendix B), and the virial relation, $M_{\text{BH}} = f_c c \tau_{\text{obs}} \text{FWHM}^2/G$, where c is the speed of light and G the gravitational constant.

The dimensionless accretion rate (\dot{M}) was introduced by Wang et al. (2014a) assuming a Shakura–Sunyaev (SS) disk. Originally, \dot{M} is adjusted for the continuum at 5100 Å, and therefore it must be rescaled for other wavelengths. Following

the standard SS accretion disk, we get

$$\dot{M} = \alpha \left(\frac{\lambda}{5100} \right)^{-1/2} L_{\lambda}^{3/2} M_{\text{BH}}^{-2}, \quad (3)$$

where λ is the wavelength of the continuum luminosity (L_{λ}). Comparing with the formula given by Wang et al. (2014a), \dot{M} at 3000 Å is given by

$$\dot{M} = 26.2 \left(\frac{L_{44}}{\cos \theta} \right)^{3/2} m_7^{-2}, \quad (4)$$

where L_{44} is the luminosity at 3000 Å in units of $10^{44} \text{ erg s}^{-1}$, θ is the inclination angle of disk to the line of sight, and m_7 is the black hole mass in units of $10^7 M_{\odot}$. We considered $\cos \theta = 0.75$, which is the mean disk inclination for type 1 AGNs and is in agreement with the typical torus covering factor found (e.g., Lawrence & Elvis 2010; Ichikawa et al. 2015).

Previously, in Zajaček et al. (2020) we used the \dot{M} definition adjusted for 5100 Å; therefore, the \dot{M} values reported there must be rescaled simply multiplying by a factor of 1.3038. The corrected \dot{M} values for the Zajaček et al. (2020) sample are already included in Table B1.

The Eddington ratio is defined as $L_{\text{bol}}/L_{\text{Edd}} = bc \cdot L_{3000}/L_{\text{Edd}}$, where $bc = 5.62 \pm 1.14$ (Richards et al. 2006) and $L_{\text{Edd}} = 1.5 \times 10^{38} \left(\frac{M_{\text{BH}}}{M_{\odot}} \right)$. In Table B1, we report the dimensionless accretion rates and the Eddington ratios. We use both the dimensionless accretion rate and the Eddington ratio since it is not clear which of these two dimensionless values is determined more accurately. Eddington ratio requires the knowledge of the broadband spectrum or use of the bolometric correction, which neglects, for example, the spin issue in a quasar and is based on a specific spectral energy distribution (SED) shape. The \dot{M} determination does not require the knowledge of the bolometric correction, but the dependence on the black hole mass determination is much stronger than for the Eddington ratio, and the spectral slope in the quasar might not be consistent with the theoretical power law expected from the Shakura & Sunyaev (1973) accretion disk model.

3. Results

3.1. Standard Radius–Luminosity Relation

First, we use the full reverberation-mapped Mg II sample and study the relation between the measured time delay of the Mg II line and the continuum flux at 3000 Å. In Figure 1 (top left panel), a clear linear trend is visible, although the rms scatter, defined using the sample size N , observed values τ_i , and predicted values $\hat{\tau}_i$ as

$$\sigma_{\text{rms}} = \sqrt{\frac{1}{N} \sum_{i=1}^N (\tau_i - \hat{\tau}_i)^2}, \quad (5)$$

is considerable, with $\sigma_{\text{rms}} = 0.3014$ dex. The best-fit parameters are given in Table 1, where we also give the values of the rms scatter and the Pearson correlation coefficient (r). The correlation is moderately strong but clearly visible. The scatter is visibly larger than in Zajaček et al. (2020), where only 11 sources were available and the R – L relation for all the available sources at that time had a scatter of $\sigma_{\text{rms}} = 0.22$ dex and $\sigma_{\text{rms}} = 0.19$ dex when two sources with the largest offset were removed. The slope is now also much shallower than given by

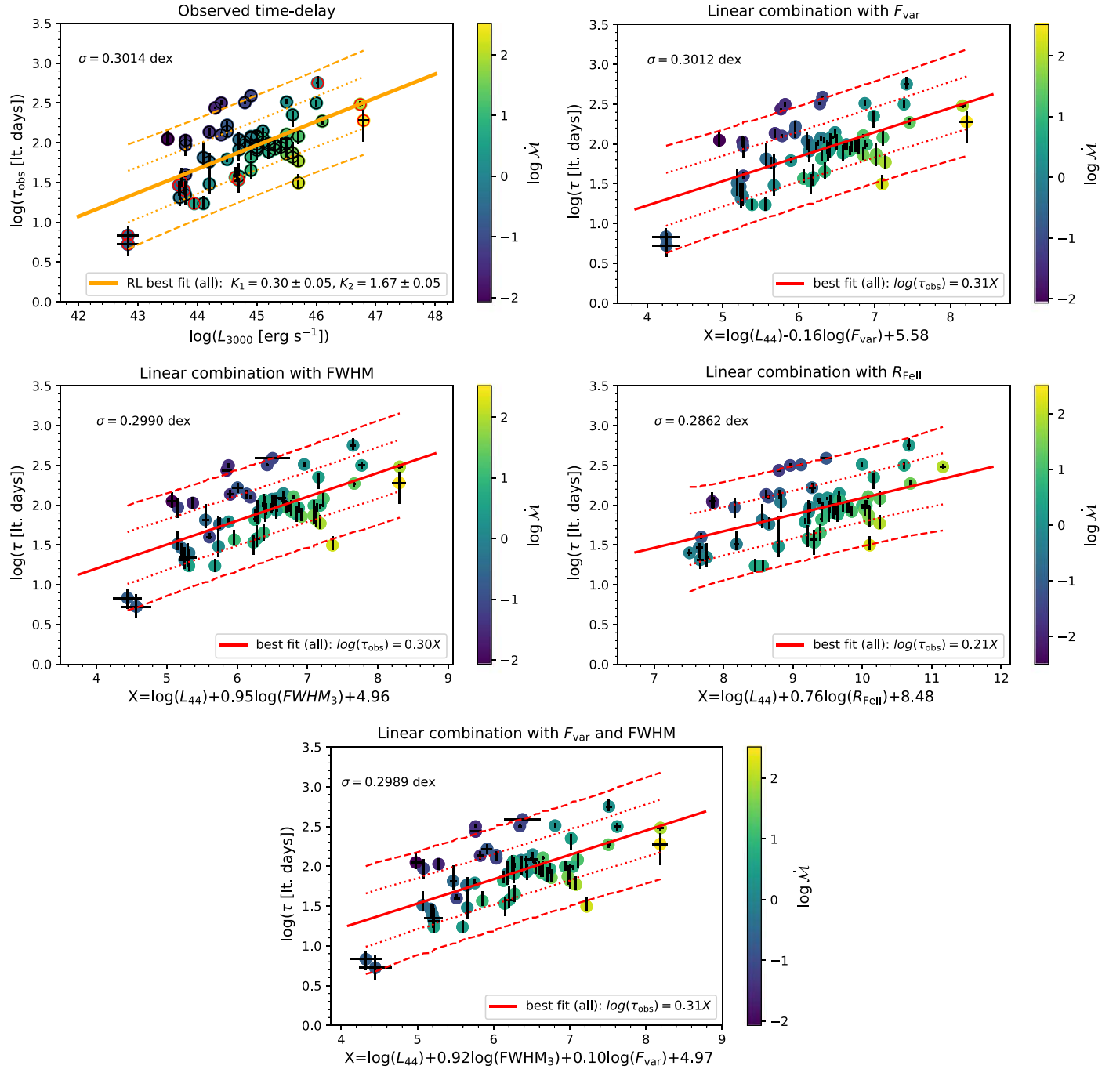


Figure 1. Observed time delay (τ_{obs}) expressed as a linear combination of the monochromatic luminosity at 3000 Å (top left panel), of luminosity L_{44} and F_{var} parameter (top right panel), of L_{44} and FWHM (middle left panel), of L_{44} and $R_{\text{Fe II}}$ (middle right panel), and of L_{44} , FWHM, and F_{var} parameters (bottom panel). These combinations have a comparable scatter of 0.3 dex. Dotted and dashed lines denote the 68% and 95% confidence intervals, respectively. The color code represents the intensity of the dimensionless accretion rate, $\lambda \dot{M}$.

Zajaček et al. (2020) (0.42 ± 0.05 for all 11 sources and 0.58 ± 0.07 with two outliers removed; see their Figure 5, right panel) or obtained earlier by McLure & Jarvis (2002) at the basis of the Mg II line shape. The R – L luminosity in the past was much better studied for the H β time delay with respect to the continuum at 5100 Å, and then the slope was close to 0.5 when the host contamination was carefully taken into account (e.g., Bentz et al. 2013). The correlation for the Mg II line is partially (but not entirely) driven by the extreme points representing the

lowest (NGC 4151) and the highest (CTS C30.10, HE 0413-4031 and CTS 252) luminosity sources.

Since it is generally accepted now that the large dispersion is related to the range of dimensionless accretion rates (Du et al. 2016; Yu et al. 2020b; Zajaček et al. 2020), we mark the points in the plot with the color, corresponding to $\lambda \dot{M}$ values. A certain degree of dependence is visible, but the trend is not at all clear—yellow points occupy mostly the lower part of the diagram, but they also concentrate more toward higher values

Table 1

Results of the Parameter Inference Applied to the Logarithm of the Observed Time Delay (τ_{obs}) Expressed as a Linear Combination of the Logarithm of the Monochromatic Luminosity (Expressed as L_{3000} or L_{44}) and Other Quantities

Sample	Inference	$\log \tau_{\text{obs}} =$	K_1	K_2	K_3	K_4 or f	σ_{rms} [dex]	r
All	OLS	$K_1 \log L_{44} + K_2$	0.298 ± 0.047	1.670 ± 0.053	0.3014	0.62
Low	OLS	$K_1 \log L_{44} + K_2$	0.520 ± 0.078	1.732 ± 0.056	0.2815	0.76
High	OLS	$K_1 \log L_{44} + K_2$	0.414 ± 0.058	1.382 ± 0.085	0.2012	0.78
All	OLS	$K_1 \log L_{44} + K_2 \log \text{FWHM}_3 + K_3$	0.30 ± 0.05	0.29 ± 0.28	1.49 ± 0.18	...	0.2990	0.63
Low	OLS	$K_1 \log L_{44} + K_2 \log \text{FWHM}_3 + K_3$	0.54 ± 0.08	-0.59 ± 0.40	2.12 ± 0.27	...	0.2722	0.78
High	OLS	$K_1 \log L_{44} + K_2 \log \text{FWHM}_3 + K_3$	0.42 ± 0.06	-0.12 ± 0.32	1.44 ± 0.17	...	0.2007	0.78
All	OLS	$K_1 \log L_{44} + K_2 \log \dot{M} + K_3$	0.694 ± 0.022	-0.432 ± 0.018	1.442 ± 0.019	...	0.0947	0.97
All	MCMC	$K_1 \log L_{44} + K_2 \log \dot{M} + K_3$	$0.6965^{+0.0102}_{-0.0098}$	$-0.4550^{+0.0054}_{-0.0054}$	$1.4618^{+0.0124}_{-0.0128}$...	0.0985	0.97
All	MCMC (f)	$K_1 \log L_{44} + K_2 \log \dot{M} + K_3$	$0.6984^{+0.0236}_{-0.0234}$	$-0.4558^{+0.0127}_{-0.0125}$	$1.4600^{+0.0297}_{-0.0293}$	$f = 2.3730^{+0.2292}_{-0.1916}$	0.0985	0.97
All	OLS	$K_1 \log L_{44} + K_2 \log L/L_{\text{Edd}} + K_3$	0.910 ± 0.029	-0.863 ± 0.035	0.380 ± 0.056	...	0.0947	0.97
All	OLS	$K_1 \log L_{44} + K_2 \log R_{\text{Fe II}} + K_3$	0.21 ± 0.06	0.16 ± 0.16	1.77 ± 0.07	...	0.2862	0.51
Low	OLS	$K_1 \log L_{44} + K_2 \log R_{\text{Fe II}} + K_3$	0.27 ± 0.11	0.35 ± 0.18	1.92 ± 0.08	...	0.2521	0.68
High	OLS	$K_1 \log L_{44} + K_2 \log R_{\text{Fe II}} + K_3$	0.47 ± 0.06	1.04 ± 0.33	1.25 ± 0.08	...	0.1718	0.84
High	MCMC	$K_1 \log L_{44} + K_2 \log R_{\text{Fe II}} + K_3$	$0.4749^{+0.0177}_{-0.0178}$	$1.0647^{+0.1120}_{-0.1146}$	$1.2678^{+0.0327}_{-0.0328}$...	0.1743	0.85
High	MCMC (f)	$K_1 \log L_{44} + K_2 \log R_{\text{Fe II}} + K_3$	$0.4761^{+0.0404}_{-0.0397}$	$1.0735^{+0.2663}_{-0.2725}$	$1.2659^{+0.0718}_{-0.0751}$	$f = 2.3420^{+0.3458}_{-0.2671}$	0.1743	0.85
All	OLS	$K_1 \log L_{44} + K_2 \log F_{\text{var}} + K_3$	0.307 ± 0.056	0.048 ± 0.178	1.712 ± 0.165	...	0.3012	0.62
Low	OLS	$K_1 \log L_{44} + K_2 \log F_{\text{var}} + K_3$	0.550 ± 0.087	0.173 ± 0.223	1.879 ± 0.198	...	0.2788	0.77
High	OLS	$K_1 \log L_{44} + K_2 \log F_{\text{var}} + K_3$	0.370 ± 0.058	-0.406 ± 0.179	0.980 ± 0.194	...	0.1863	0.82
All	OLS	$K_1 \log L_{44} + K_2 \log \text{FWHM}_3 + K_3 \log F_{\text{var}} + K_4$	0.306 ± 0.056	0.280 ± 0.282	0.032 ± 0.178	$K_4 = 1.522 \pm 0.252$	0.2989	0.63

Note. We analyze parameter values and the scatter for the whole Mg II sample (denoted as “All”) or its low- or high-accretion subsamples (denoted as “Low” or “High,” respectively), which is specified in the first column. The parameter inference type—ordinary least squares (OLS) or Markov Chain Monte Carlo (MCMC)—is specified in the second column. The third column lists the analyzed parameter combination. The other columns contain coefficient values with standard errors within 1σ , rms scatter (σ_{rms}) along the linear relations in dex, and the Pearson correlation coefficient (r). For the two cases with the smallest rms scatter, namely, combinations with $\log L_{44}$, $\log \dot{M}$ and $\log L_{44}$, $\log R_{\text{Fe II}}$, we perform MCMC fitting to cross-check our linear regression results with and without the underestimation factor f , which, if included, is listed in the same column as the K_4 coefficient.

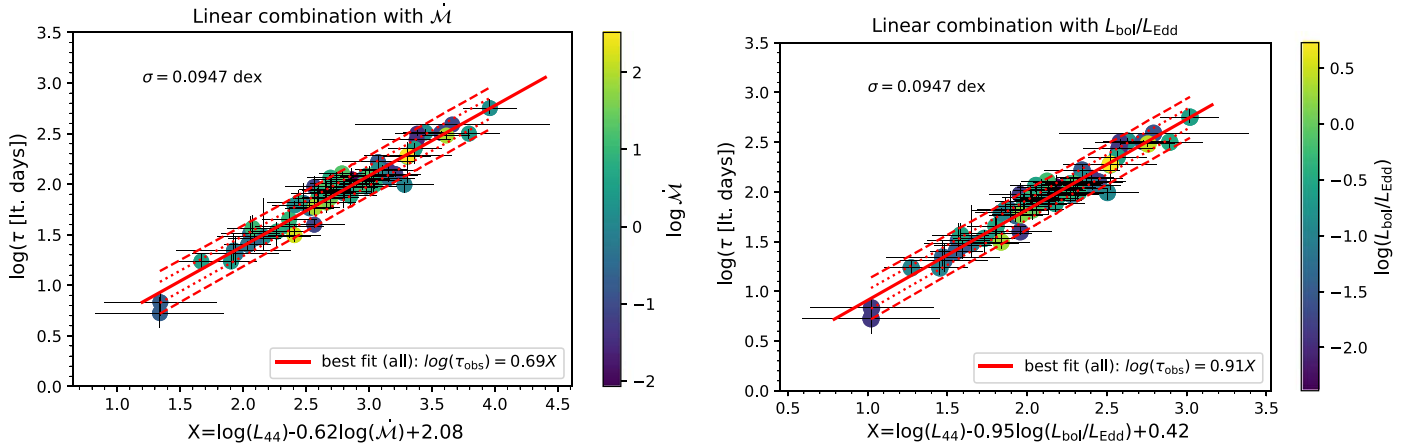


Figure 2. Observed time delay (τ_{obs}) as a function of the linear combination of L_{44} and \dot{M} (left panel) and of L_{44} and $L_{\text{bol}}/L_{\text{Edd}}$ (right panel). The scatter along the linear relation is comparable in both cases, $\sigma_{\text{rms}} \sim 0.1$ dex. Dotted and dashed lines denote the 68% and 95% confidence intervals, respectively. The color code represents the intensity of the dimensionless accretion rate, \dot{M} .

of the luminosity. Zajaček et al. (2020) achieve the considerable reduction of the scatter when the observed time delay was corrected for the trend with \dot{M} or $L_{\text{bol}}/L_{\text{Edd}}$, particularly if the virial factor f_c depending on FWHM (Mejía-Restrepo et al. 2018; Martínez-Aldama et al. 2019) instead of a constant value has been used. In their work, Lusso & Risaliti (2017) use the additional dependence on FWHM to reduce the scatter in their quasar relation between the X-ray and the UV flux, and Du & Wang (2019) and Yu et al. (2020b) applied the additional dependence on the \dot{M} and $R_{\text{Fe II}}$ to reduce the scatter in the R – L relation for $\text{H}\beta$. Thus, we can expect that including more parameters in the fit will lead to the reduction in the scatter to a smaller or larger extent.

3.2. Scatter Reduction Using a Linear Combination of Variables

The need to reduce the large scatter along the R – L relation motivates us to search for extended, multidimensional radius–luminosity relations that involve linear combinations of the logarithms of monochromatic luminosity (L_{44}) with additional parameters, which can generally be written as $\log \tau_{\text{obs}} = K_1 \log L_{44} + \sum_{i=2}^n K_i \log Q_i + K_{n+1}$, where the parameters Q_i are typically related to the accretion rate and we use \dot{M} , $L_{\text{bol}}/L_{\text{Edd}}$, F_{var} , and $R_{\text{Fe II}}$ for this purpose. The total number of quantities is typically $n = 2$; in a few cases we have $n = 3$. FWHM is either included or in some cases omitted from the linear combination. An overview of all studied cases is in Table 1 (third column).

We use the Python packages `sklearn` and `statsmodels` to perform a multivariate linear regression and to obtain regression coefficients K_1 , K_i , and K_{n+1} , including their standard errors, and the correlation coefficients (r), which are listed in Table 1 for each linear combination. In addition, we also include the rms scatter calculated using Equation (5).

We list all the relations in Table 1, and graphically they are shown in Figures 1 and 2. In these figures, for an easier comparison of the slopes $\tau_{\text{obs}} \propto L_{44}^\alpha$, we plot $\log \tau_{\text{obs}}$ versus $\log L_{44} + \sum_{i=2}^n K_i/K_1 \log Q_i + K_{n+1}/K_1$, where K_1 represents the slope α .

The smallest scatter of $\sigma_{\text{rms}} \sim 0.1$ dex is for combinations that include L_{44} and either \dot{M} or $L_{\text{bol}}/L_{\text{Edd}}$ (see Figure 2). When, in addition to \dot{M} or $L_{\text{bol}}/L_{\text{Edd}}$, FWHM is added to the

combination, the scatter is of the order of $\sigma_{\text{rms}} \sim 10^{-4}$ dex only. However, in this case, the correlation is artificially enhanced (the correlation coefficient is essentially 1.00), as both \dot{M} and $L_{\text{bol}}/L_{\text{Edd}}$ depend on τ_{obs} and FWHM via the black hole mass. The use of such interdependent quantities is not welcome, as that may easily create an apparent correlation, and the subsequent error determination when such a relation is used has to take that into account. For this reason, we do not include these two cases in the overview of linear combinations in Table 1.

Considering independent quantities like FWHM, $R_{\text{Fe II}}$, and F_{var} decreases the scatter, but the effect is relatively small and is comparable to the original R – L relation for Mg II , $\sigma_{\text{rms}} \sim 0.3$ dex (see Figure 1). The scatter drops by 0.8% when FWHM is added to L_{44} and only by 0.07% when F_{var} is added to L_{44} . This is not a significant improvement in terms of the scatter, but the relations define planes instead of a line and thus connect three or four independent observables, which can be relevant in terms of understanding mutual relations among them.

An additional dependence on $R_{\text{Fe II}}$ gives a better result: the scatter drops from 0.3 dex down to 0.286 dex (see Table 1), but the correlation coefficient also drops, so apparently $R_{\text{Fe II}}$ adds considerably to the scatter. Also, the slope of the relation is shallower. Although $R_{\text{Fe II}}$ and F_{var} are physically related to the Eddington ratio, neither of these quantities leads to the considerable improvement when the whole sample is considered.

Combining even more quantities does not provide an improvement either: a combination of L_{44} , FWHM, F_{var} , and $R_{\text{Fe II}}$ still leads to almost the same scatter and the same value of the correlation coefficient as in the basic R – L relation. Other combinations also do not provide an improvement.

3.3. Sample Division: Low and High Accretors

To make use of the strong dependence on \dot{M} in the reduction of the scatter in Section 3.2, we divided the full sample into two subsamples: low and high accretors. Although limits for low and high accretors have previously been discussed (e.g., Marziani et al. 2003; Du et al. 2015), in this work we consider a division that gives us the subsamples containing comparable numbers of objects. Thus, as a

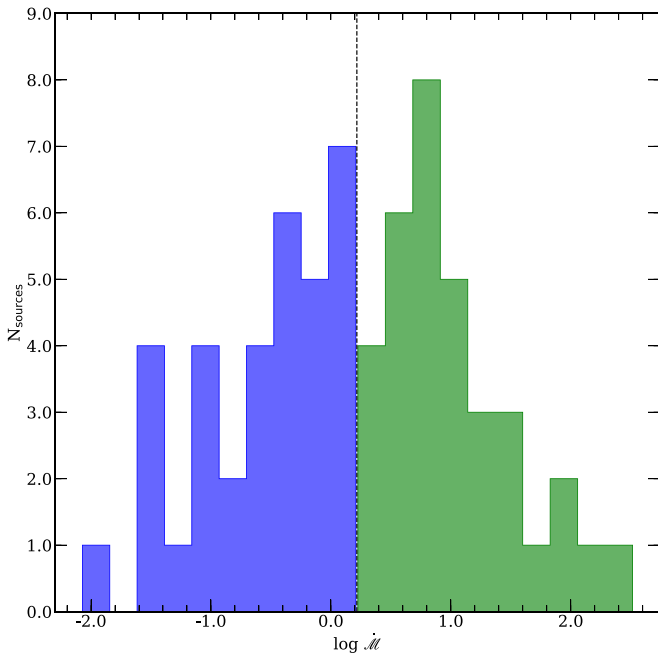


Figure 3. Dimensionless accretion rate distribution for the full sample. Blue and green histograms represent the low and high accretion subsamples, respectively. The vertical line indicates the median \dot{M} value for the full sample, $\log \dot{M} = 0.2167$.

reference, we consider the median \dot{M} value ($\log \dot{M} = 0.2167$) to get an equal number of sources (34 objects) in each subsample. In Figure 3, the \dot{M} distribution is shown for low and high accretors. In Section 4.3, we include a discussion of the accretion rates observed in our sample in a general context considering samples like the DR7 (Shen et al. 2011) and DR14 (Rakshit et al. 2020), which also support the \dot{M} division considered in this work.

The division of the sample into high and low accretors results in significantly reducing the scatter, particularly for the highly accreting subsample (see Table 1 and Figure 4). It is also interesting to note that the slopes in the R – L relation in both subsamples are steeper than for the whole sample and much closer to the theoretically expected value of 0.5. Comparing both cases, for low accretors, the slope is steeper, closer to the canonical 0.5 value than for the highly accreting subsample, but the difference is within the quoted slope errors.

The Pearson correlation coefficient increased significantly for both subsamples, supporting the view that mixing sources with different accretion rates spoils the pattern. The dispersion in both subsamples decreased in comparison with the whole sample, but here the effect in the two subsamples is clearly different. In the low- \dot{M} subsample, the reduction in the dispersion is not that strong, from 0.3 dex down to 0.28 dex. However, the drop in the dispersion for the highly accreting sources is spectacular, from 0.3 dex to 0.2 dex. We should stress here again that this division has been set at $\dot{M} = 1.65$, and the definition of \dot{M} does not include the accretion efficiency, so for a standard efficiency of 10% this corresponds to mild accretion rates above 0.165 in dimensionless units. Hence, a considerable fraction of quasars in the SDSS-RM objects (Homayouni et al. 2020) belong to this category (see Section 4.3).

For the low accretion rate subsample, our dispersion in the R – L relation for Mg II is still higher than the dispersion of 0.19 dex obtained by Bentz et al. (2013) for R – L in $H\beta$, without the removal of outliers. However, our sources are, on average, brighter than those in Bentz et al. (2013), where most of the sources are at $\log L_{5100} \sim 43.5$, and we study a different emission line. For high accretion rate sources, our dispersion is comparable to Bentz et al. (2013), and we did not remove any outliers in our analysis. Removing outliers (e.g., by 3σ clipping) would clearly tighten the correlation, but we use the data from the literature and we do not think we can reliably eliminate some of the available measurements. This shows that for Mg II quasar population the highly accreting sources are much more attractive for cosmological applications.

We also studied the subsamples allowing for additional parametric dependencies: FWHM, $R_{\text{Fe II}}$, and F_{var} . The inclusion of FWHM in the fit gave some further decrease of the dispersion, but the effect is not strong (see bottom panels of Figure 4). Concerning the fractional variability F_{var} , for the low-accretion sources, the improvement was marginal in comparison with the base R – L relation for these sources; see Figure 5 (bottom left panel). However, moving toward the highly accreting subsample, the reduction in scatter is significant, down to 0.19 dex (see Figure 5, bottom right panel), and the correlation coefficient also increased. An even larger reduction in the scatter was achieved when we included $R_{\text{Fe II}}$ (see Figure 5, top panels). The effect was clearly visible for both subsamples, and for the high accretion rate subsample, our dispersion reduced to only 0.17 dex, again without the removal of any outliers. This was the smallest scatter achieved in our study without the use of interdependent quantities.

3.4. Ordinary Least Squares vs. MCMC Inference of Parameters

For all the studied relations $\log \tau_{\text{obs}} = K_1 \log L_{44} + \sum_{i=2}^n K_i \log Q_i + K_{n+1}$ listed in Table 1, we used the higher-dimensional ordinary least squares (OLS) method (2D or 3D including the constant factor) as implemented in Python packages `sklearn` and `statsmodels`. This allowed us to quickly infer the relevant parameters including standard errors and compare the rms scatter and the correlation coefficient for as many as 15 combinations of relevant quantities. However, hidden correlations between quantities are not apparent when using the multidimensional least squares. Therefore, for the relations with the smallest scatter below 0.2 dex, specifically $\log \tau_{\text{obs}} = K_1 \log L_{44} + K_2 \log \dot{M} + K_3$ (whole sample) and $\log \tau_{\text{obs}} = K_1 \log L_{44} + K_2 \log R_{\text{Fe II}} + K_3$ (highly accreting sources), we apply the Markov Chain Monte Carlo (MCMC) inference of parameters, using the Python sampler `emcee`. The two inference techniques—OLS and MCMC—are specified in the second column of Table 1. The MCMC is a robust Bayesian technique that takes into account measurement errors while inferring the parameters with the maximum likelihood, which in our case is defined as

$$\mathcal{L} = -\frac{1}{2} \sum_{i=1}^N \left(\frac{\tau_i - \hat{\tau}_i}{\sigma_i^T} \right)^2, \quad (6)$$

where τ_i are individual time delay measurements, σ_i^T are the measurement errors of the time delay, and $\hat{\tau}_i$ are the predicted time delay values according to the inferred model. In addition,

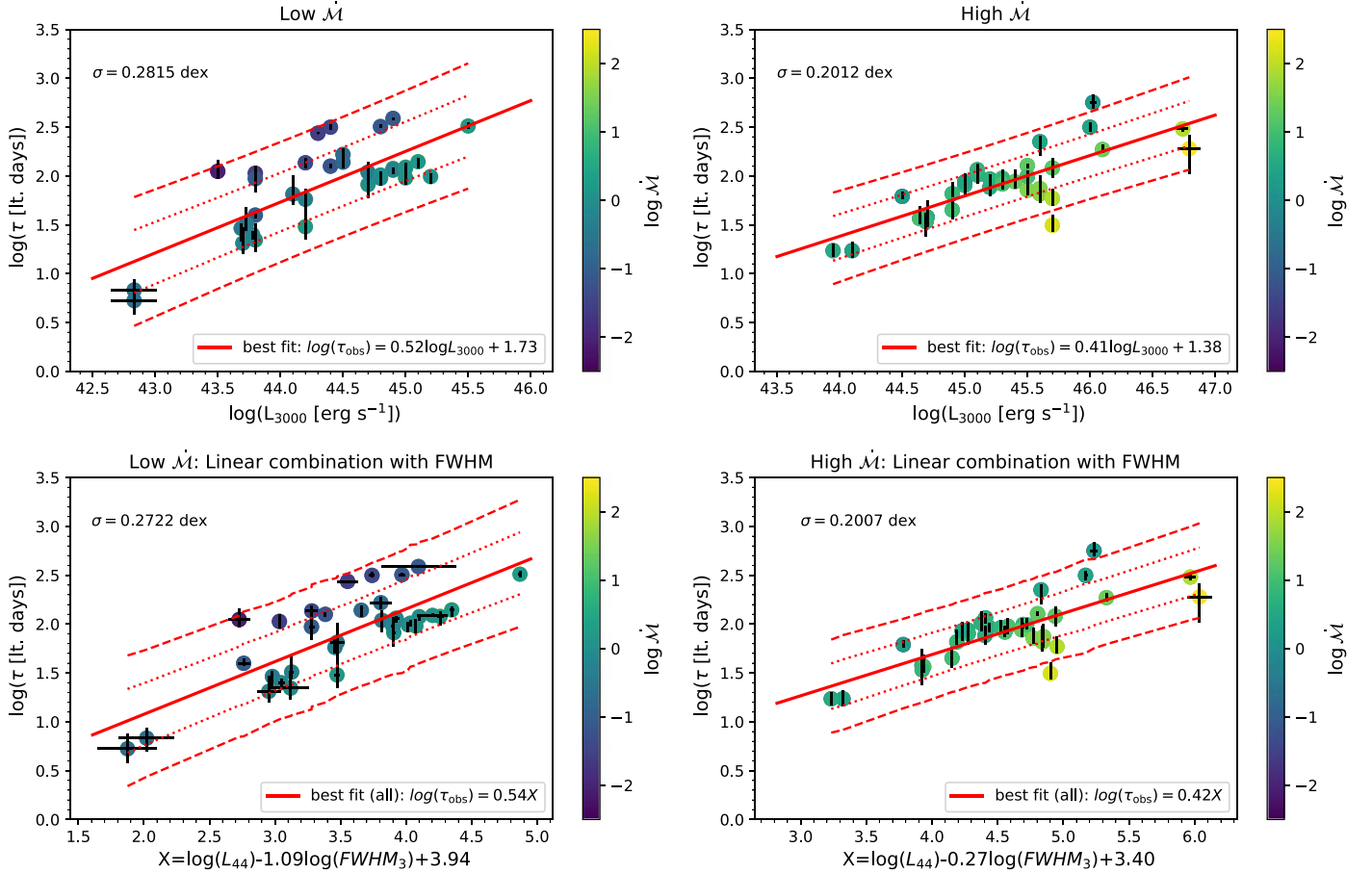


Figure 4. Observed time delay (τ_{obs}) expressed as a function of the monochromatic luminosity L_{3000} (top panels) and as a function of the linear combination $\log L_{44} + (K_2/K_1)\log FWHM_3 + (K_3/K_1)$ (bottom panels), where $FWHM_3$ indicates that the FWHM is in units of 10^3 km s^{-1} . In addition, we divide the Mg II sample into low accretors (left panels) and high accretors (right panels); see Section 3.3. Dotted and dashed lines denote the 68% and 95% confidence intervals, respectively. The color code represents the intensity of the dimensionless accretion rate, \dot{M} .

MCMC allows us to construct 2D histograms to see potential degeneracies among different parameters.

The results for the two above-mentioned relations are shown in Figure 6 for the combination including \dot{M} in the left panels and for the combination including $R_{\text{Fe II}}$ in the right panels. From 2D histograms we can see that the combination with \dot{M} exhibits a degeneracy between the constant K_3 coefficient and K_1 coefficient, as well as between the K_3 and K_2 coefficients. This can be understood in terms of \dot{M} being intrinsically correlated with τ_{obs} . The degeneracy between the K_3 and K_2 parameters is lifted for the combination with $R_{\text{Fe II}}$, as $R_{\text{Fe II}}$ and τ_{obs} are intrinsically not correlated.

As can be seen from the bottom panels of Figure 6, the parameters with the maximum likelihood are consistent with the best-fit parameters from the least-squares technique. The rms scatter and correlation coefficients are also comparable within uncertainties; see Table 1. However, the MCMC uncertainties based on the 16th and 84th percentiles (1σ) are smaller by a factor of about two than the 1σ errors inferred using the OLS for the combination involving \dot{M} ; see Table 1. Similarly, for the combination with $R_{\text{Fe II}}$, the reduction in uncertainty is by almost a factor of three. It may seem that the MCMC inference using the maximization of the likelihood function defined by Equation (6) is more robust for constraining individual parameters even for general priors of uniformly

distributed coefficients in the studied linear combinations. However, the likelihood function defined by Equation (6) considers only the measurement errors of τ_i . When we take into account that the measurement errors σ_i^T could generally be underestimated by a factor f , then the likelihood function takes the following form:

$$\mathcal{L}_f = -\frac{1}{2} \sum_{i=1}^N \left[\frac{(\tau_i - \hat{\tau}_i)^2}{s_i^2} + \log s_i^2 + \log(2\pi) \right], \quad (7)$$

where $s_i = f\sigma_i^T$. Maximizing the functional \mathcal{L}_f that depends on the additional underestimation parameter f yields the posterior 2D and 1D marginalized distributions as shown in Figure 7. The parameter uncertainties are now comparable to those inferred using the OLS method; see Table 1, where we list the parameters inferred using the likelihood function \mathcal{L}_f under the abbreviation MCMC(f). The difference between uncertainties inferred using either \mathcal{L} or \mathcal{L}_f shows the importance of the defined likelihood function for a given problem. In our case, the OLS and MCMC methods are in better agreement in terms of the uncertainties when the factor f is included, which suggests that the measurement time delay uncertainties are underestimated by a factor of about two or three.

Since OLS and MCMC can be considered as independent inference techniques, their overall consistency confirms the

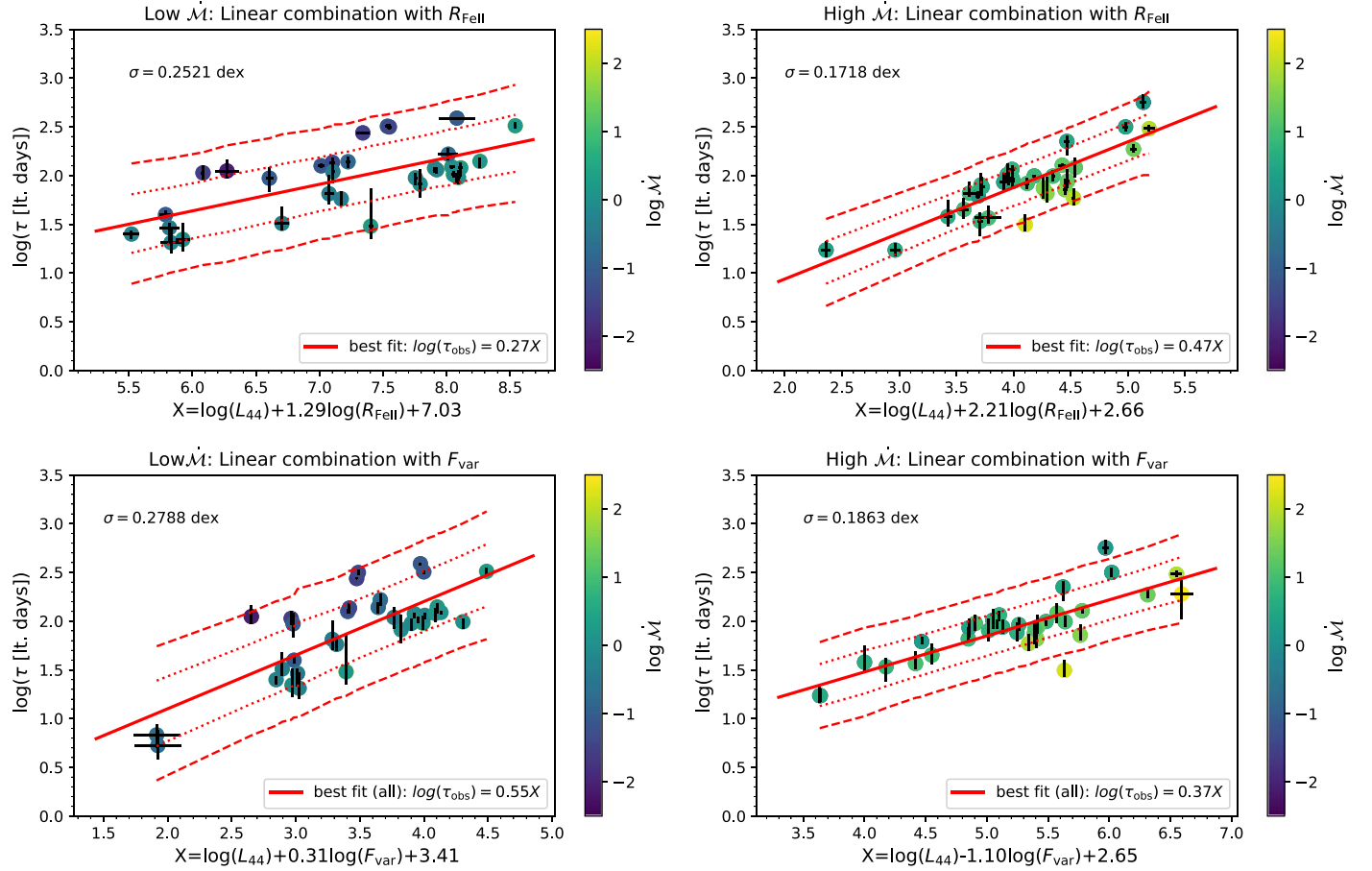


Figure 5. Observed time delay (τ_{obs}) expressed as a function of the linear combination of $\log L_{44}$ and $\log R_{\text{Fe II}}$ or $\log F_{\text{var}}$. Using the accretion rate distribution in Figure 3, we separately analyze the low accretors (top left panel) and the high accretors (top right panel), for which we obtained a significantly reduced scatter. In comparison with the previous samples, three sources are not included because of the lack of the EW measurements (CTS 252 and two measurements for NGC 4151). In the bottom panels, we show the dependency of the observed time delay on the combination including the fractional variability F_{var} for the low- (bottom left panel) and high- \dot{M} subsamples (bottom right panel). Similarly as for the combination including $R_{\text{Fe II}}$, the scatter is significantly smaller in comparison with the whole sample. Dotted and dashed lines denote the 68% and 95% confidence intervals, respectively. The color code represents the intensity of the dimensionless accretion rate, \dot{M} .

statistical robustness of our results, mainly concerning the low scatter for highly accreting sources.

4. Discussion

4.1. Mg II Radius–Luminosity Relation

The R – L relation is of key importance for black hole mass measurements in the sources that were not studied through reverberation mapping. It is also a promising tool to be applied in cosmology if we have a large enough sample showing a small scatter around the best-fit relation. In the present paper, we studied the R – L relation based on the Mg II line, using all available data, and we focused on the selection of additional parameters/methods that help to reduce the observed scatter.

Considering a virialized and photoionized gas, it is expected that $\log \tau_{\text{obs}} \propto \alpha \log L$, where the slope of the luminosity is given by $\alpha = 0.5$. In the optical range, the H β reverberation mapping results give a slope for the optical luminosity at 5100 Å of $\alpha = 0.533^{+0.035}_{-0.033}$ in the most accepted R – L relation (Bentz et al. 2013). This slope was nicely consistent with simple predictions of the BLR location based on a fixed ionization parameter (see Czerny et al. 2019b and the references therein) or the failed radiatively accelerated dusty outflow (FRADO) model (Czerny & Hryniewicz 2011).

The slope of the R – L relation based on the Mg II line shows a large diversity (Vestergaard & Osmer 2009; Trakhtenbrot & Netzer 2012; Homayouni et al. 2020; Zajaček et al. 2020). The most recent Mg II monitoring from the SDSS-RM project (Homayouni et al. 2020), which increased significantly the number of Mg II time lags, provides an R – L relation with a shallower slope than that seen for the H β line by Bentz et al. (2013). Based on their time delay significance criteria, the SDSS-RM sample (Homayouni et al. 2020) is divided into two subsamples (significant and gold sample), where the slope of the luminosity in both cases is 0.22 ± 0.06 and $0.31^{+0.09}_{-0.10}$, respectively.

In this work we combine the data of Homayouni et al. (2020) with the low- and high-luminosity sources collected by Zajaček et al. (2020). When all the measurements of Mg II delay up to now are included, we get a slope of 0.298 ± 0.047 , which is in agreement with the one inferred by Homayouni et al. (2020). However, when the sample is divided based on the median \dot{M} intensity, the slope becomes much steeper. In the case of the low-accretion subsample, the slope is very close (0.520 ± 0.078) to the expected value and the one provided by H β results. As we mentioned previously, most of the first H β reverberation-mapped objects were selected based on their high variability (high F_{var}) and strong [O III] $\lambda\lambda 5007, 4959$ emission, which indicates a low accretion rate and is expected to

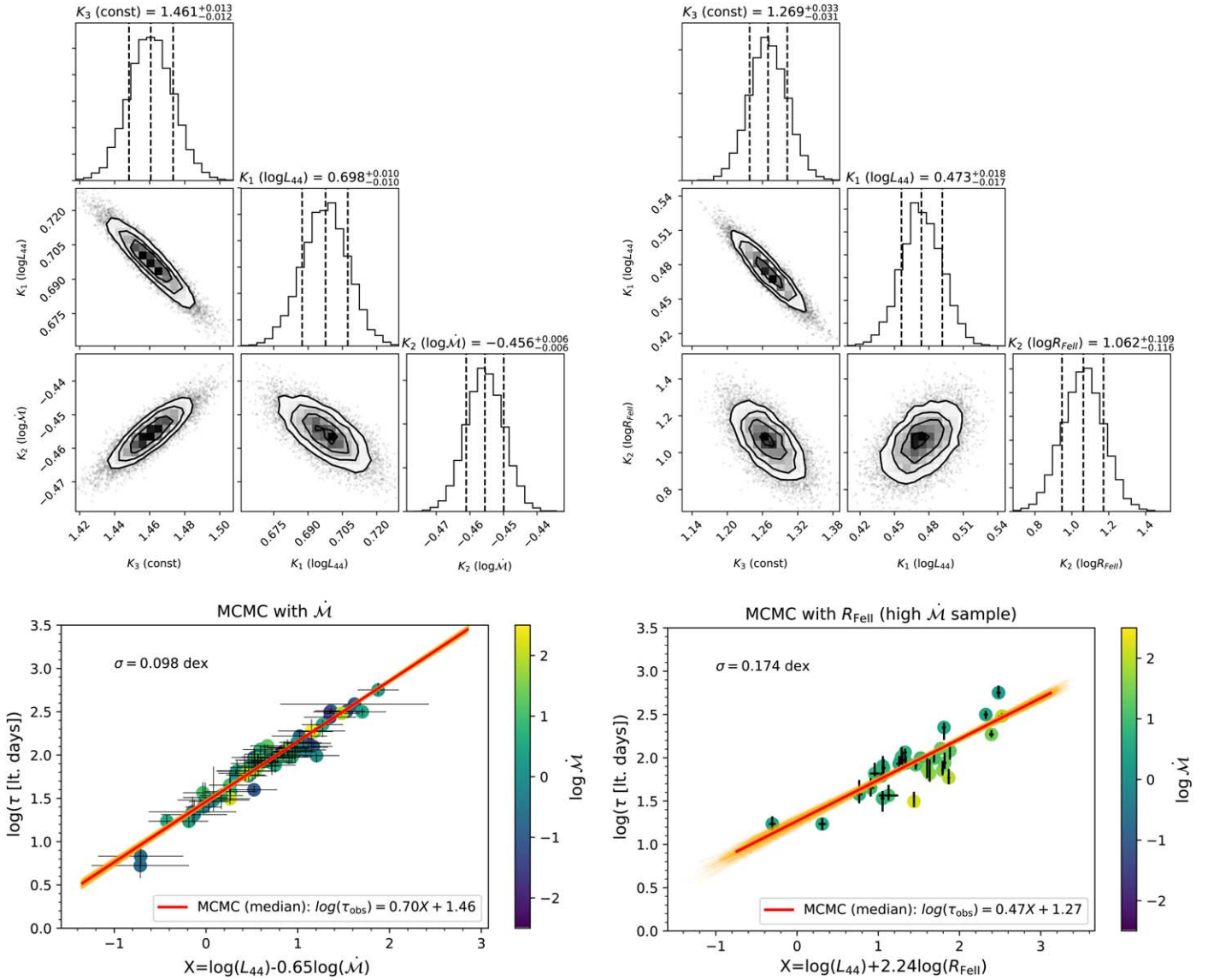


Figure 6. Histograms of the MCMC fitting to the selected combinations of variables with the smallest scatter (top panels). In the top left panel, we show the distributions for the L_{44} and \dot{M} variables. In the top right panel, the distributions for L_{44} and $R_{\text{Fe II}}$ are shown. In the bottom panels, we show the corresponding linear relations between the observed time delay and the linear combination of variables. In the bottom left panel, the relation between $\log \tau_{\text{obs}}$ and $\log L_{44} + A \log \dot{M}$ is depicted. The red line represents the maximum likelihood linear relation, while the set of orange lines stands for 300 relations drawn from posterior distributions. In the bottom right panel, we plot the linear relation in analogy to the left panel, but for the observed time delay expressed as the linear combination of $\log L_{44}$ and $\log R_{\text{Fe II}}$ for the high-accretion subsample.

show an agreement with the standard slope. In the case of the high- \dot{M} subsample, the slope is 0.414 ± 0.058 , which, within uncertainties, is very close to the expected value. A large sample of highly accreting objects is needed to confirm a real deviation of the slope of the luminosity for this kind of object.

When additional independent observational parameters are considered in linear combinations with the luminosity at 3000 \AA , the slope shows different values. Since the typical slope of 0.5 is estimated considering only the luminosity, we cannot claim a deviation from it in the other studied cases where $R_{\text{Fe II}}$, F_{var} , and FWHM are used, because new theoretical models taking into account these parameters should be considered.

4.2. The Role of the Accretion Rate in Reducing the Scatter

Newer, larger samples for the $\text{H}\beta$ line brought an additional scatter in comparison with the sample of Bentz et al. (2013),

and also the scatter in the Mg II full sample is relatively large, $\sigma_{\text{rms}} \sim 0.3$ dex. However, a more advanced approach presented in this paper helped to reduce this scatter considerably. The smallest scatter has been achieved when interdependent quantities (\dot{M} and $L_{\text{bol}}/L_{\text{Edd}}$) are used. These results, thus, have to be treated with care since they are intrinsically correlated with the time delay. On one hand, it is an attractive hypothesis that the scatter in the original R – L relation (i.e., $\log \tau_{\text{obs}}$ vs. $\log L_{44}$) is due to the spread in the accretion rate intensity. The underlying mechanism for shortening the time delay with an increase in the accretion rate has already been suggested by Wang et al. (2014c), who argued that the self-shielding of the accretion disk also leads to the selective shielding of the BLR and its division into two distinctly different regions. In addition, within the FRADO model combined with the shielding effect, such a trend is expected (Naddaf et al. 2020).

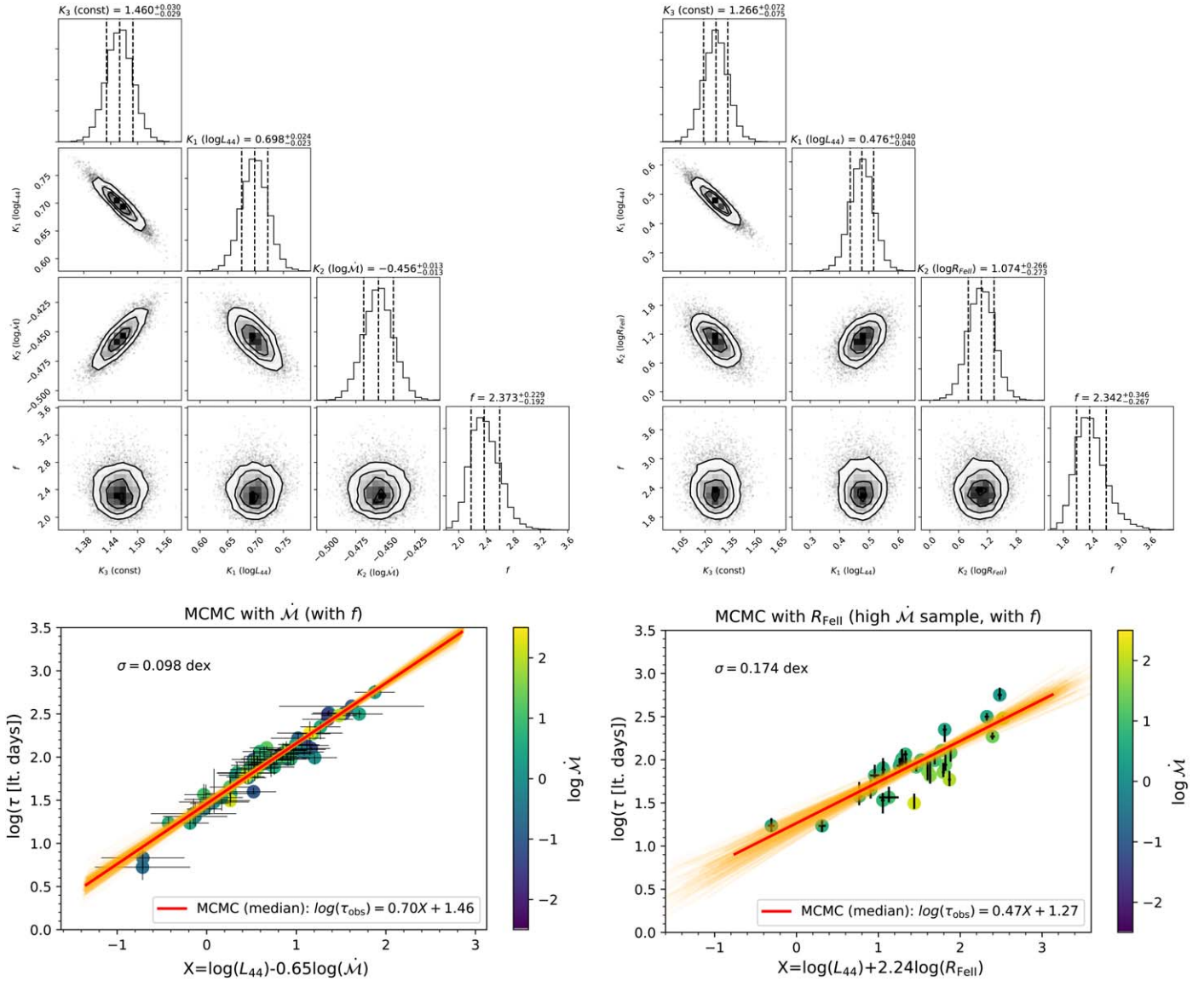


Figure 7. Same MCMC fitting procedure as in Figure 6, but including the underestimation factor f in the likelihood function; see Equation (7).

The use of the interdependent quantities has a drawback, that, despite the small scatter in the final plot, the recovery of the values predicted by the relation comes with a large error. If we want to use the linear combination with \dot{M} (left panel in Figure 2; see also Table 1, rows 7 and 8) to predict the value of the time delay for a given source, if we measure the FWHM and the L_{44} assuming a known cosmology, the error of this prediction will become larger than the scatter visible in the plot: the minimum value of the error of $\log \tau_{\text{obs}}$ in this case would be $\delta K_3 / 0.136 = 0.147$, where δK_3 is the error of the coefficient K_3 in Table 1, row 7. The same will happen if we use the linear combination with \dot{M} (left panel of Figure 2) to obtain the absolute luminosity from the measured time delay and FWHM—the minimum error of the predicted $\log L_{44}$ would then be $\delta K_3 / 0.046 = 0.43$. Thus, for the black hole mass measurements or for the cosmological applications, the use of the relations based on independent quantities still gives much better results. An attractive possibility would be to use the accretion rate or the Eddington ratio as independent parameters. This would require an independent measurement of the black

hole mass, e.g., from the broadband SED fitting (Capellupo et al. 2015).

The use of the MCMC fitting method with the interdependent \dot{M} parameter reduces the error for all the coefficients, so the numbers mentioned above will be formally up to 3 times lower. However, the dispersion around the fit is not affected by the inference method, so it is not clear whether the use of MCMC indeed reduces the errors when predictions are made. As we also showed in Section 3.4, the uncertainty intervals of the posterior parameter distributions also depend on whether the underestimation parameter is included in the likelihood function or not. If it is included, then the uncertainties are consistent with the OLS method, which suggests that the time delay uncertainties are generally underestimated by about a factor of two.

The dominant role of the dimensionless accretion rate or the Eddington ratio is supported by the fact that the division of the sample into two parts representing low and high accretion rates also reduced the scatter in the R – L relation considerably, particularly for the case of the highly accreting subsample. In combination with the measurement of $R_{\text{Fe II}}$, this reduced the

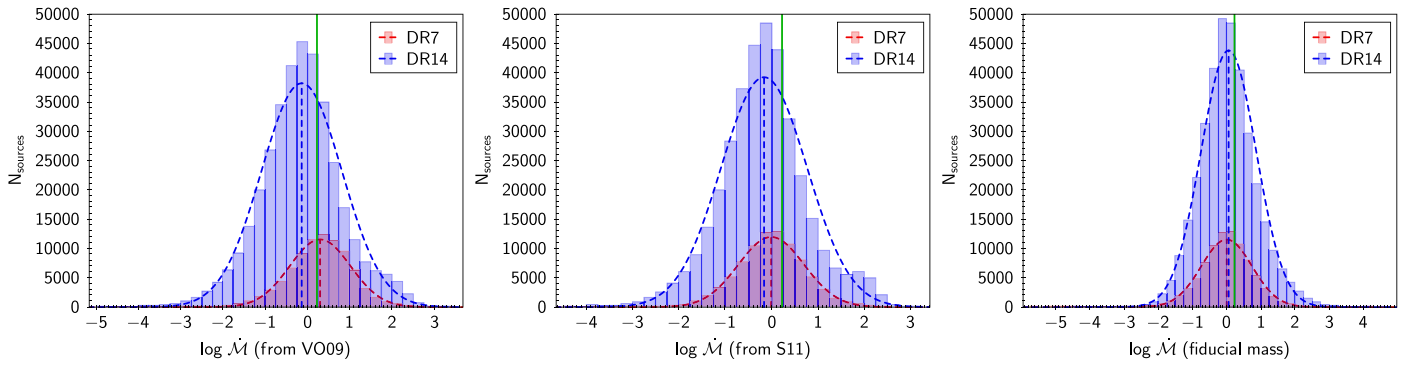


Figure 8. Distribution of \dot{M} (in log scale) for two representative editions: DR7 (Shen et al. 2011) and DR14 (Rakshit et al. 2020). The \dot{M} values are estimated using Equation (4). The first two panels represent the formalisms for the estimation of the black hole mass using the Mg II line from (a) Vestergaard & Osmer (2009) and (b) Shen et al. (2011). The last panel reports the \dot{M} using the fiducial masses reported in the two catalogs. Gaussian fits (dashed curves) to the histograms are shown with mean values marked (vertical dashed lines). No radiative efficiency has been accounted. The $(\mu \pm \sigma)$ values for each panels are (a) 0.29 ± 0.72 (DR7) and -0.14 ± 0.95 (DR14), (b) -0.02 ± 0.71 (DR7) and -0.17 ± 0.93 (DR14), and (c) -0.01 ± 0.74 (DR7) and 0.05 ± 0.81 (DR14). The green solid vertical line in each panel indicates the \dot{M} value for our sample, $\log \dot{M} = 0.2167$.

scatter in the R – L relation down to ~ 0.17 dex. The scatter for the lower accretion rate subsample remained at $\sigma_{\text{rms}} \sim 0.25$ dex. This level of scatter is most likely related to the red-noise character of AGN variability in the optical band (e.g., Czerny et al. 1999; Kelly et al. 2009; Kozłowski et al. 2010; Kozłowski 2016). A relatively short monitoring allows one to determine the time delay of the lines with respect to the continuum, but years of monitoring are needed to determine the mean luminosity level, instead of a part of the light curve catching the source in a relatively high or a relatively low state. As was shown by Ai et al. (2010) for SDSS Stripe 82 AGNs, higher Eddington ratio sources vary less in the optical/UV bands. This variability, in particular for a low-accretion subsample, may lead to an irreducible scatter in the R – L relation, as is clearly seen for our results (Figures 4 and 5). The same scatter was discussed by Risaliti & Lusso (2019) in the context of the broadband UV–X-ray relation, where they argue that the variability is relatively unimportant for high-redshift quasars, leading to the scatter of 0.04 dex. However, their selection of predominantly blue quasars contributed to the reduction of this scatter. During the 16 yr quasar monitoring, the variability varied from 0.04 to 0.1 dex, depending on the quasar absolute luminosity (Hook et al. 1994). In our sample, no preselection of objects based on the UV slope has been made.

Alternatively, the reduction in the scatter in the subsample with high \dot{M} could be related to the fact that sources radiating close to their Eddington limit saturate toward a limiting value, which leads to the stabilizing of the ratio between the luminosity and black hole mass (which is basically \dot{M} or $L_{\text{bol}}/L_{\text{Edd}}$), making the sources steadier (Marziani & Sulentic 2014). Other explanations of the additional scatter include the spin effect and the possibility of a retrograde accretion (Wang et al. 2014b; Czerny et al. 2019b).

We stress the fact that $R_{\text{Fe II}}$ and F_{var} show the smallest scatter (0.17 and 0.19 dex, respectively) when the sample is divided into the two considering the \dot{M} intensity. Both observational properties are correlated with \dot{M} and $L_{\text{bol}}/L_{\text{Edd}}$ (Marziani et al. 2003; Wilhite et al. 2008; Dong et al. 2009, 2011; MacLeod et al. 2010; Sánchez-Sáez et al. 2018; Martínez-Aldama et al. 2019; Du & Wang 2019; Yu et al. 2020b), but they are independent. This result suggests that the accretion rate drives the scatter in the R – L relation.

4.3. \dot{M} Behavior in Larger Samples

The division based on the \dot{M} for the current sample could be affected by inclusion of newer sources or reanalyses of existing ones. As a check for completeness, we compare the distribution of \dot{M} estimated for two large SDSS quasar catalogs—for the DR7 release (Shen et al. 2011, hereafter S11) and for a more recent DR14 release (Rakshit et al. 2020, hereafter R20), with various spectral parameters estimated for 105,783 and 526,265 sources, respectively. The \dot{M} formalism used in this paper (see Equation (4)) is a function of the black hole mass and the monochromatic luminosity at 3000 Å (the associated inclination term, $\cos \theta$, is set to 0.75, which is the mean disk inclination for type 1 AGNs). We filter the catalogs first by limiting to the values that are reported to be positive and nonzero. Additionally, in the latter case (R20), the authors also provide quality flags for selected parameters including the monochromatic luminosity at 3000 Å (L_{3000}). For the DR7 QSO catalog, no such quality flags were provided; thus, we use the full sample in this case. For the black holes masses, we use three variants common to the two catalogs: (a) from Vestergaard & Osmer (2009, hereafter VO09), (b) from S11, and (c) from the fiducial virial black hole mass values calculated based on (a) the H β line (for $z > 0.8$) using the calibration of Vestergaard & Peterson (2006), (b) the Mg II line (for $0.8 \leq z < 1.9$) using the calibration provided by VO09, and (c) the C IV line (for $z \geq 1.9$) using the Vestergaard & Peterson (2006) calibration. In the case of the black hole masses, the DR14 QSO catalog provides the quality flag only for the fiducial masses and is unavailable for the VO09 and S11 mass estimates. We thus use the quality flags to control the sample for the fiducial mass estimates in this case. Figure 8 demonstrates the \dot{M} distributions computed for the two catalogs. The three panels are synonymous to the three cases of black hole mass estimates incorporated to estimate the \dot{M} values.

Due to the quality control and filtering, the source sample drops to $\sim 79\%$ (DR7) and to $\sim 67\%$ (DR14) of their respective original source counts. The effective numbers of sources per case of the black hole mass estimates remain almost alike.³ To predict the variation with respect to our small sample of Mg II

³ For the DR7 QSO catalog, the \dot{M} values were estimated for 83,374 sources with M_{BH} from VO09, for 85,099 sources with M_{BH} from S11, and for 85,638 sources with fiducial masses. Equivalently, for the DR14 QSO catalogs, these numbers are over 4 times larger—365,440 sources with M_{BH} each from VO09 and S11, and for 354,675 sources with fiducial masses.

RM-reported sources, we extract the mean (μ) and the standard deviation (σ) from each \dot{M} distribution (in log scale) shown in Figure 8 using simple Gaussian fits. The ($\mu \pm \sigma$) values for each panels are (VO09) 0.29 ± 0.72 (DR7) and -0.14 ± 0.95 (DR14), (S11) -0.02 ± 0.71 (DR7) and -0.17 ± 0.93 (DR14), and (fiducial) -0.01 ± 0.74 (DR7) and 0.05 ± 0.81 (DR14). The median value for our sample, $\log \dot{M} = 0.2167$, is well within 1σ limits regardless of the distribution taken from the larger catalogs, and hence it will not have significant effects on the correlations quoted in this paper with the inclusion of more sources in the future.

5. Conclusions

Using a sample of 68 reverberation-mapped Mg II AGNs, we explore the reasons for the scatter along the R – L relation. In addition to the dimensionless accretion rate parameter \dot{M} and the Eddington ratio, we included independent parameters such as FWHM of Mg II, F_{var} , and $R_{\text{Fe II}}$ in linear combinations with the luminosity (L_{3000} or L_{44}) to decrease the scatter. We summarize the important conclusions derived from this analysis as follows:

1. When the whole Mg II sample is considered, we find the smallest rms scatter of $\sigma_{\text{rms}} \sim 0.1$ dex for the combinations that include both the monochromatic luminosity (L_{3000}) and either the dimensionless accretion rate parameter \dot{M} or the Eddington ratio ($L_{\text{bol}}/L_{\text{Edd}}$). However, for these combinations, there is a caveat that both \dot{M} and $L_{\text{bol}}/L_{\text{Edd}}$ are intrinsically correlated with the time delay. Despite the fact that the scatter decreases significantly, the determination of the time delay or luminosity using the proposed linear combinations provides values with larger errors (for both the OLS and MCMC inference techniques).
2. The inclusion of independent parameters such as FWHM, $R_{\text{Fe II}}$, and F_{var} in the linear combination with the luminosity at 3000 Å leads to a slight decrease of the scatter. In all of the analyzed cases, the scatter ($\sigma_{\text{rms}} \sim 0.3$ dex) and the correlation coefficients are similar.
3. For the whole sample, the slope of the luminosity at 3000 Å is less steep ($\alpha = 0.298 \pm 0.047$) than the expected value of ~ 0.5 . However, after the division of the sample considering the \dot{M} intensity, low- \dot{M} sources follow the expected behavior, while the high- \dot{M} sources show a slightly shallower slope, and the relation is shifted toward shorter time delays. This manifests the effect of the accretion in the R – L relation.
4. When the sample is divided into low- and high- \dot{M} subsamples, the scatter decreases significantly and the correlation coefficient increases, in particular for the highly accreting subsample. The case with the smallest scatter is the combination including $R_{\text{Fe II}}$ with the scatter of only $\sigma_{\text{rms}} \sim 0.17$ dex. Also, the inclusion of F_{var} results in a low scatter, $\sigma_{\text{rms}} \sim 0.19$ dex, which is of interest for future photometric surveys. Since $R_{\text{Fe II}}$ and

F_{var} are independent and at the same time correlated with the accretion rate, our results support the idea that the scatter in the R – L relation is driven by the accretion rate intensity. In particular, F_{var} has a potential applicability in the upcoming surveys, such as the Legacy Survey of Space and Time (LSST; see Ivezić et al. 2019), which will provide a large quantity of photometric data. The established relations with physical parameters, such as the accretion rate intensity, could be used as a tool for the classification of sources.

The authors would like to acknowledge the anonymous referee for the very helpful comments and suggestions. We acknowledge the financial support by the National Science Centre, Poland, grant No. 2017/26/A/ST9/00756 (Maestro 9), and by the Ministry of Science and Higher Education (MNiSW) grant DIR/WK/2018/12. Time delay for two quasars reported in this paper were obtained with the Southern African Large Telescope (SALT). Polish participation in SALT is funded by grant No. MNiSW DIR/WK/2016/07.

Software: sklearn (Pedregosa et al. 2011); statsmodels (Seabold & Perktold 2010); emcee (Foreman-Mackey et al. 2013); numpy (Oliphant 2015); matplotlib (Hunter 2007); TOPCAT (Taylor 2005).

Appendix A Relation between the UV Fe II and the Accretion Parameters

According to our analysis, the linear combinations of the luminosity at 3000 Å and the strength of the UV Fe II (expressed as $R_{\text{Fe II}}$) decrease significantly the scatter in the R – L relation. The inclusion of the $R_{\text{Fe II}}$ parameter is justified by the correlation with the accretion parameters (Dong et al. 2011), and it is also suggested by the similar behavior shown in the optical range. Since the optical emission and the UV Fe II emission are anticorrelated with the FWHM of H β (Kovačević-Dojčinović & Popović 2015; Śniegowska et al. 2020), and in the optical case it is widely shown that this relation is driven by the accretion rate (e.g., Marziani et al. 2003; Shen & Ho 2014; Du & Wang 2019, and references therein), it suggests that for the UV case this should hold as well.

Figure A1 shows the relation between $R_{\text{Fe II}}$ and the dimensionless accretion rate (left panel) and the Eddington ratio (right panel). As a reference, we include the Mg II measurements from the catalog of Shen et al. (2019), where $L_{\text{bol}}/L_{\text{Edd}}$ was taken from the catalog and \dot{M} was estimated from the single-epoch black hole mass based on Mg II reported in that paper. Figure A1 also includes the Spearman correlation coefficient (ρ) and p -values, which indicate a weak correlation between both parameters, but slightly stronger than the correlations found by Dong et al. (2009). Although the correlation is weak, this result opens the possibility to explore this relation in the future and justifies the inclusion of the UV Fe II in the linear combinations presented in this paper.

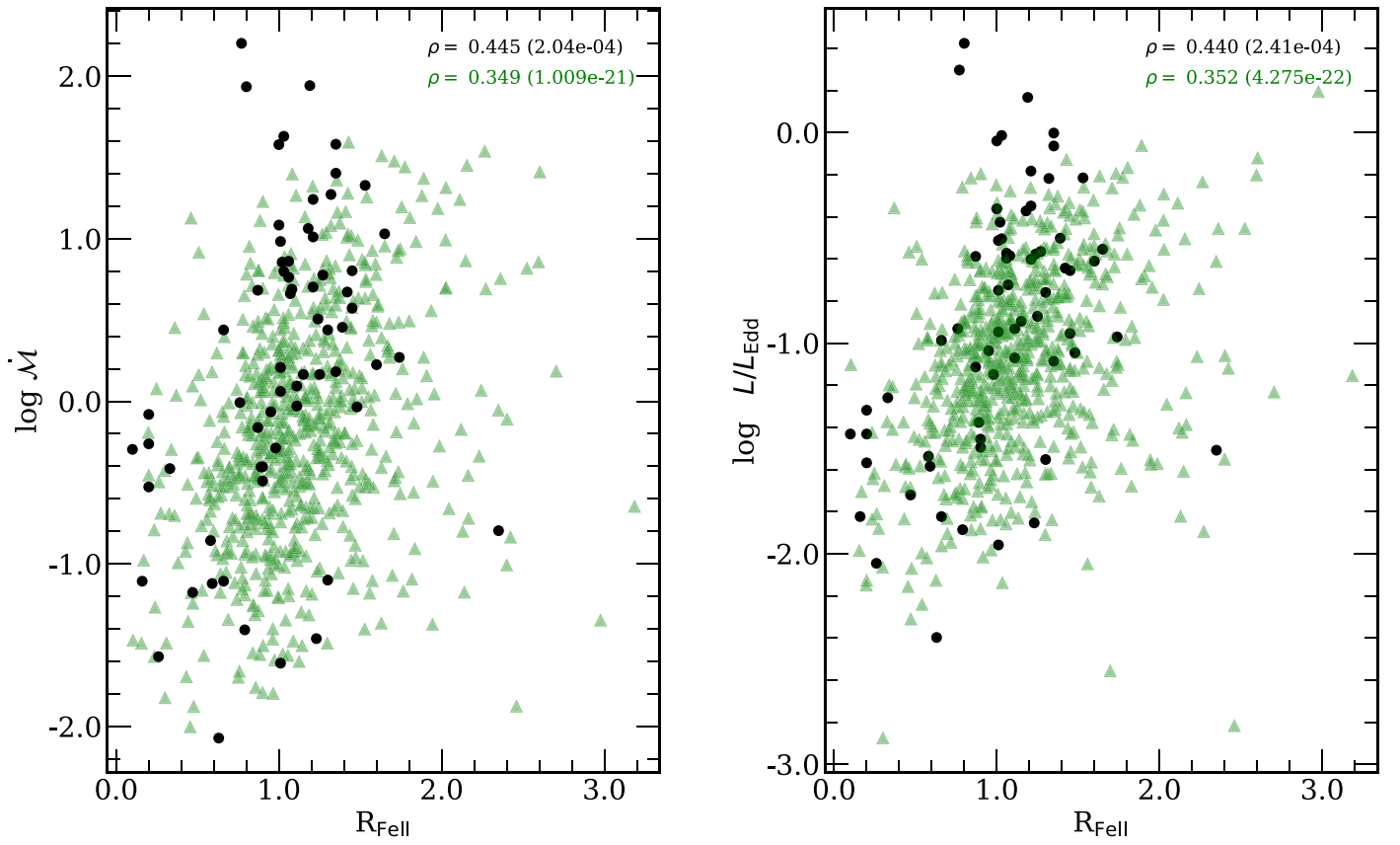


Figure A1. Relation between the R_{Fell} parameter and the dimensionless accretion rate (left panel) and the Eddington ratio (right panel). Black symbols correspond to the presented sample, while green symbols mark the sources from the Shen et al. (2019) catalog. In both panels, the Spearman coefficient and p -value are included for both samples.

Appendix B

Observational Properties for the Full Sample

In this section, we summarize the observational properties for the full sample used in the analysis. The description of the columns is included in the notes of Table B1.

Table B1
Observational Properties for the Full Sample

Object	$\log L_{3000}$ (erg s ⁻¹)	τ_{obs} (1 lt-day)	FWHM Mg II (km s ⁻¹)	$\log \dot{\mathcal{M}}$	$L_{\text{bol}}/L_{\text{Edd}}$	$R_{\text{Fe II}}$	F_{var}	Class
(1)	(2)	(3)	(4)	(5)	(6)	(7)	(8)	(9)
SDSS-RM Sample (Homayouni et al. 2020)								
18	44.4 ± 0.0009	125.9 ^{+6.8} _{-7.0}	7416 ± 123	-1.176 ^{+0.321} _{-0.321}	0.019 ^{+0.008} _{-0.008}	0.470 ± 0.019	0.050	1
28	45.6 ± 0.0004	65.7 ^{+24.8} _{-14.2}	3899 ± 75	1.630 ^{+0.328} _{-0.424}	0.968 ^{+0.511} _{-0.415}	1.030 ± 0.013	0.088	2
38	45.7 ± 0.0003	120.7 ^{+27.9} _{-28.7}	3954 ± 87	1.242 ^{+0.340} _{-0.336}	0.656 ^{+0.287} _{-0.289}	1.210 ± 0.015	0.077	2
44	44.9 ± 0.0013	65.8 ^{+18.8} _{-4.8}	2583 ± 114	0.861 ^{+0.288} _{-0.375}	0.267 ^{+0.127} _{-0.104}	1.060 ± 0.064	0.066	2
102	45.0 ± 0.0005	86.9 ^{+16.2} _{-13.3}	2977 ± 78	0.672 ^{+0.299} _{-0.313}	0.227 ^{+0.094} _{-0.091}	1.420 ± 0.026	0.045	2
114	46.1 ± 0.0003	186.6 ^{+20.3} _{-15.4}	4318 ± 226	1.403 ^{+0.299} _{-0.305}	0.994 ^{+0.403} _{-0.397}	1.350 ± 0.040	0.038	2
118	45.1 ± 0.0006	102.2 ^{+27.0} _{-19.5}	2885 ± 64	0.703 ^{+0.314} _{-0.352}	0.250 ^{+0.113} _{-0.104}	1.210 ± 0.027	0.066	2
123	44.7 ± 0.0009	81.6 ^{+28.0} _{-26.6}	4647 ± 126	-0.029 ^{+0.398} _{-0.408}	0.085 ^{+0.044} _{-0.043}	1.110 ± 0.032	0.117	1
135	45.2 ± 0.0005	93.0 ^{+9.6} _{-9.8}	4128 ± 64	0.689 ^{+0.285} _{-0.284}	0.260 ^{+0.100} _{-0.100}	1.080 ± 0.010	0.075	2
158	44.9 ± 0.0012	119.1 ^{+4.0} _{-11.8}	4699 ± 69	-0.065 ^{+0.289} _{-0.278}	0.092 ^{+0.035} _{-0.036}	0.950 ± 0.021	0.058	1
159	45.5 ± 0.0006	324.2 ^{+25.3} _{-19.4}	3298 ± 87	0.208 ^{+0.273} _{-0.277}	0.178 ^{+0.067} _{-0.067}	1.010 ± 0.018	0.044	1
160	43.8 ± 0.0013	106.5 ^{+18.2} _{-16.6}	4386 ± 56	-1.571 ^{+0.303} _{-0.310}	0.009 ^{+0.004} _{-0.004}	0.260 ± 0.005	0.160	1
170	45.2 ± 0.0005	98.5 ^{+6.7} _{-17.7}	10594 ± 121	-0.008 ^{+0.395} _{-0.368}	0.117 ^{+0.055} _{-0.058}	0.760 ± 0.011	0.103	1
185	44.9 ± 0.0094	387.9 ^{+3.3} _{-3.0}	4765 ± 2835	-1.100 ^{+1.239} _{-1.239}	0.028 ^{+0.040} _{-0.040}	1.300 ± 0.326	0.082	1
191	43.8 ± 0.0012	93.9 ^{+24.3} _{-29.1}	2619 ± 109	-1.107 ^{+0.388} _{-0.358}	0.015 ^{+0.007} _{-0.007}	0.660 ± 0.034	0.178	1
228	44.7 ± 0.0011	37.9 ^{+14.4} _{-9.1}	4481 ± 460	0.662 ^{+0.401} _{-0.475}	0.189 ^{+0.111} _{-0.095}	1.070 ± 0.042	0.256	2
232	44.3 ± 0.0014	273.8 ^{+5.1} _{-4.1}	4202 ± 713	-1.611 ^{+0.436} _{-0.436}	0.011 ^{+0.006} _{-0.006}	1.010 ± 0.090	0.173	1
240	44.1 ± 0.0021	17.2 ^{+3.5} _{-2.8}	4547 ± 126	0.439 ^{+0.312} _{-0.330}	0.103 ^{+0.045} _{-0.043}	0.660 ± 0.028	0.157	2
260	45.3 ± 0.0004	94.9 ^{+18.7} _{-17.2}	2814 ± 90	1.084 ^{+0.314} _{-0.321}	0.434 ^{+0.183} _{-0.180}	1.000 ± 0.018	0.135	2
280	45.5 ± 0.0003	99.1 ^{+3.3} _{-9.5}	5751 ± 256	0.856 ^{+0.315} _{-0.305}	0.375 ^{+0.152} _{-0.156}	1.020 ± 0.014	0.061	2
285	44.5 ± 0.0020	138.5 ^{+15.2} _{-21.1}	5139 ± 65	-0.857 ^{+0.311} _{-0.297}	0.029 ^{+0.012} _{-0.012}	0.580 ± 0.019	0.137	1
291	43.8 ± 0.0016	39.7 ^{+4.2} _{-2.6}	7788 ± 761	-1.107 ^{+0.382} _{-0.389}	0.015 ^{+0.007} _{-0.007}	0.160 ± 0.012	0.188	1
294	45.5 ± 0.0004	71.8 ^{+17.8} _{-9.5}	3008 ± 52	1.581 ^{+0.289} _{-0.342}	0.863 ^{+0.382} _{-0.337}	1.350 ± 0.025	0.034	2
301	44.2 ± 0.0011	136.3 ^{+17.0} _{-16.9}	6052 ± 599	-1.406 ^{+0.373} _{-0.373}	0.013 ^{+0.006} _{-0.006}	0.790 ± 0.027	0.239	1
303	44.2 ± 0.0013	57.7 ^{+10.5} _{-8.3}	4173 ± 95	-0.404 ^{+0.300} _{-0.315}	0.042 ^{+0.017} _{-0.017}	0.890 ± 0.017	0.114	1
329	45.4 ± 0.0007	87.5 ^{+23.8} _{-14.0}	2720 ± 29	1.328 ^{+0.300} _{-0.355}	0.609 ^{+0.278} _{-0.244}	1.530 ± 0.033	0.057	2
338	43.8 ± 0.0013	22.1 ^{+8.8} _{-6.2}	3662 ± 1102	-0.081 ^{+0.708} _{-0.750}	0.048 ^{+0.043} _{-0.040}	0.200 ± 0.019	0.168	1
419	45.0 ± 0.0011	95.5 ^{+15.2} _{-15.5}	6132 ± 135	0.094 ^{+0.330} _{-0.329}	0.117 ^{+0.050} _{-0.050}	1.110 ± 0.026	0.046	1
422	44.7 ± 0.0011	109.3 ^{+25.4} _{-29.6}	5628 ± 94	-0.414 ^{+0.373} _{-0.353}	0.055 ^{+0.025} _{-0.026}	0.330 ± 0.007	0.078	1
440	44.9 ± 0.0004	114.6 ^{+7.4} _{-10.8}	6825 ± 403	-0.288 ^{+0.339} _{-0.334}	0.071 ^{+0.031} _{-0.031}	0.980 ± 0.014	0.105	1
441	45.5 ± 0.0004	127.7 ^{+5.7} _{-7.3}	2276 ± 91	1.272 ^{+0.288} _{-0.286}	0.605 ^{+0.234} _{-0.235}	1.320 ± 0.042	0.033	2
449	45.0 ± 0.0013	119.8 ^{+14.7} _{-24.4}	4149 ± 216	0.165 ^{+0.338} _{-0.307}	0.127 ^{+0.052} _{-0.056}	1.150 ± 0.034	0.091	1
457	43.7 ± 0.0029	20.5 ^{+7.7} _{-5.3}	4213 ± 810	-0.262 ^{+0.524} _{-0.575}	0.037 ^{+0.025} _{-0.023}	0.200 ± 0.028	0.524	1
459	45.0 ± 0.0011	122.8 ^{+5.1} _{-5.7}	4686 ± 1134	0.061 ^{+0.564} _{-0.564}	0.113 ^{+0.076} _{-0.076}	1.010 ± 0.035	0.127	1
469	45.6 ± 0.0002	224.1 ^{+27.9} _{-74.3}	4246 ± 57	0.506 ^{+0.395} _{-0.291}	0.265 ^{+0.104} _{-0.132}	1.240 ± 0.029	0.056	2
492	45.3 ± 0.0004	92.0 ^{+16.3} _{-12.7}	4436 ± 103	0.799 ^{+0.300} _{-0.315}	0.313 ^{+0.130} _{-0.125}	1.030 ± 0.017	0.064	2
493	46.0 ± 0.0004	315.6 ^{+30.7} _{-35.7}	7102 ± 823	0.455 ^{+0.402} _{-0.399}	0.315 ^{+0.158} _{-0.159}	1.390 ± 0.036	0.056	2
501	44.9 ± 0.0009	44.9 ^{+11.7} _{-10.4}	3511 ± 110	0.983 ^{+0.337} _{-0.353}	0.307 ^{+0.139} _{-0.135}	1.010 ± 0.044	0.123	2
505	44.8 ± 0.0011	94.7 ^{+10.8} _{-16.7}	5819 ± 160	-0.162 ^{+0.333} _{-0.312}	0.077 ^{+0.032} _{-0.034}	0.870 ± 0.021	0.101	1
522	45.1 ± 0.0006	115.8 ^{+11.3} _{-16.0}	2214 ± 33	0.776 ^{+0.300} _{-0.288}	0.272 ^{+0.106} _{-0.109}	1.270 ± 0.032	0.059	2
556	45.5 ± 0.0005	98.7 ^{+13.9} _{-10.8}	4616 ± 90	1.011 ^{+0.292} _{-0.302}	0.448 ^{+0.180} _{-0.176}	1.210 ± 0.016	0.044	2
588	45.6 ± 0.0002	74.3 ^{+23.0} _{-18.2}	3596 ± 42	1.579 ^{+0.340} _{-0.377}	0.912 ^{+0.438} _{-0.402}	1.000 ± 0.013	0.092	2
593	45.0 ± 0.0006	80.1 ^{+21.4} _{-20.8}	2890 ± 41	0.763 ^{+0.348} _{-0.352}	0.253 ^{+0.115} _{-0.114}	1.060 ± 0.018	0.057	2
622	44.5 ± 0.0005	61.7 ^{+6.0} _{-4.3}	2768 ± 128	0.270 ^{+0.287} _{-0.293}	0.107 ^{+0.042} _{-0.042}	1.740 ± 0.037	0.063	2
645	44.2 ± 0.0009	30.2 ^{+26.8} _{-8.9}	4035 ± 158	0.182 ^{+0.378} _{-0.819}	0.082 ^{+0.079} _{-0.039}	1.350 ± 0.044	0.197	1
649	44.5 ± 0.0013	165.5 ^{+22.2} _{-25.1}	3753 ± 666	-0.796 ^{+0.466} _{-0.462}	0.031 ^{+0.018} _{-0.018}	2.350 ± 0.330	0.155	1
651	45.2 ± 0.0011	76.5 ^{+18.0} _{-15.6}	5331 ± 85	0.683 ^{+0.336} _{-0.351}	0.258 ^{+0.117} _{-0.113}	0.870 ± 0.022	0.054	2


Table B1
(Continued)

Object	$\log L_{3000}$ (erg s ⁻¹)	τ_{obs} (1 lt-day)	FWHM Mg II (km s ⁻¹)	$\log \dot{\mathcal{M}}$	$L_{\text{bol}}/L_{\text{Edd}}$	$R_{\text{Fe II}}$	F_{var}	Class
(1)	(2)	(3)	(4)	(5)	(6)	(7)	(8)	(9)
675	45.1 ± 0.0005	139.8 ^{+12.0} _{-22.6}	4250 ± 132	0.165 ^{+0.310} _{-0.286}	0.134 ^{+0.052} _{-0.055}	1.250 ± 0.015	0.049	1
678	45.3 ± 0.0007	82.9 ^{+11.9} _{-10.2}	3446 ± 67	1.063 ^{+0.287} _{-0.294}	0.424 ^{+0.167} _{-0.164}	1.180 ± 0.025	0.049	2
709	45.0 ± 0.0010	85.4 ^{+17.7} _{-19.3}	4277 ± 197	0.439 ^{+0.346} _{-0.337}	0.174 ^{+0.076} _{-0.078}	1.300 ± 0.047	0.080	2
714	44.8 ± 0.0012	320.1 ^{+11.3} _{-11.2}	5031 ± 266	-1.121 ^{+0.300} _{-0.300}	0.026 ^{+0.010} _{-0.010}	0.590 ± 0.022	0.206	1
756	44.4 ± 0.0023	315.3 ^{+20.5} _{-16.4}	3505 ± 151	-1.460 ^{+0.281} _{-0.284}	0.014 ^{+0.005} _{-0.005}	1.230 ± 0.034	0.092	1
761	44.8 ± 0.0024	102.1 ^{+8.2} _{-7.4}	4393 ± 79	-0.035 ^{+0.280} _{-0.282}	0.090 ^{+0.034} _{-0.034}	1.480 ± 0.042	0.149	1
771	45.7 ± 0.0004	31.3 ^{+8.1} _{-4.6}	5391 ± 57	2.202 ^{+0.312} _{-0.363}	1.980 ^{+0.920} _{-0.818}	0.770 ± 0.008	0.068	2
774	45.7 ± 0.0004	58.9 ^{+13.7} _{-10.1}	3537 ± 125	1.942 ^{+0.311} _{-0.340}	1.468 ^{+0.647} _{-0.604}	1.190 ± 0.021	0.125	2
792	43.5 ± 0.0030	111.4 ^{+29.5} _{-20.0}	4451 ± 772	-2.072 ^{+0.474} _{-0.501}	0.004 ^{+0.003} _{-0.002}	0.630 ± 0.103	0.148	1
848	44.1 ± 0.0015	65.1 ^{+29.4} _{-16.3}	3264 ± 378	-0.490 ^{+0.414} _{-0.527}	0.035 ^{+0.023} _{-0.018}	0.900 ± 0.058	0.186	1
Zajaček et al. (2020) Sample								
J141214	44.6 ± 0.0004	36.7 ^{+10.4} _{-4.8}	2391 ± 46	1.030 ^{+0.367} _{-0.295}	0.279 ^{+0.131} _{-0.110}	1.650 ± 0.201	0.094	2
J141018	43.7 ± 0.0051	32.3 ^{+12.9} _{-5.3}	3101 ± 76	-0.403 ^{+0.438} _{-0.303}	0.032 ^{+0.017} _{-0.013}	0.900 ± 0.085	0.162	1
J141417	43.7 ± 0.0029	29.1 ^{+3.6} _{-8.8}	3874 ± 86	-0.527 ^{+0.290} _{-0.376}	0.027 ^{+0.011} _{-0.013}	0.200 ± 0.028	0.524	1
J142049	44.7 ± 0.0009	34.0 ^{+6.7} _{-12.0}	4108 ± 39	0.803 ^{+0.318} _{-0.407}	0.221 ^{+0.093} _{-0.113}	1.450 ± 0.034	0.174	2
J141650	43.8 ± 0.0020	25.1 ^{+2.0} _{-2.6}	4066 ± 202	-0.296 ^{+0.294} _{-0.299}	0.037 ^{+0.015} _{-0.015}	0.100 ± 0.011	0.080	1
J141644	43.9 ± 0.0010	17.2 ^{+2.7} _{-2.7}	2681 ± 96	0.573 ^{+0.307} _{-0.307}	0.111 ^{+0.045} _{-0.045}	1.450 ± 0.068	0.113	2
CTS 252	46.8 ± 0.0914	190.0 ^{+59.0} _{-114.0}	3800 ± 380	2.516 ^{+0.450} _{-0.634}	5.334 ^{+3.063} _{-4.109}	—	0.090	2
NGC 4151	42.8 ± 0.1821	6.8 ^{+1.7} _{-2.1}	4823 ± 1105	-0.698 ^{+0.643} _{-0.662}	0.013 ^{+0.011} _{-0.011}	—	0.088	1
NGC 4151	42.8 ± 0.1821	5.3 ^{+1.9} _{-1.8}	6558 ± 1850	-0.692 ^{+0.768} _{-0.762}	0.014 ^{+0.013} _{-0.013}	—	0.094	1
CTS C30.10	46.0 ± 0.0260	564.0 ^{+109.0} _{-71.0}	5009 ± 325	0.225 ^{+0.353} _{-0.329}	0.245 ^{+0.112} _{-0.106}	1.600 ^{+0.005} _{-0.003}	0.066	2
HE 0413-4013	46.7 ± 0.0434	302.9 ^{+23.7} _{-19.1}	4380 ± 14	1.935 ^{+0.290} _{-0.294}	2.652 ^{+1.052} _{-1.062}	0.800 ± 0.020	0.088	2

NOTES. Column (1): object identification. For SDSS-RM sample, each number corresponds to the RMID number in the original catalog (Homayouni et al. 2020). Column (2): logarithm of continuum luminosity at 3000 Å. Column (3): time delay in units of light-day. SDSS-RM time delays reported correspond to the ones obtained with the JAVELIN method. Column (4): FWHM of Mg II. Column (5): dimensionless accretion rate. Column (6): Eddington ratio. Column (7): R_{Fe} parameter. Column (8): F_{var} parameter. Column (9): classification based on the $\dot{\mathcal{M}}$ intensity; numbers 1 and 2 correspond to the low and high accretion rate subsample, respectively. See Section 3.3.

(This table is available in machine-readable form.)

ORCID iDs

Mary Loli Martínez–Aldama  <https://orcid.org/0000-0002-7843-7689>

Michal Zajaček  <https://orcid.org/0000-0001-6450-1187>

Bożena Czerny  <https://orcid.org/0000-0001-5848-4333>

Swayamtrupta Panda  <https://orcid.org/0000-0002-5854-7426>

References

- Ai, Y. L., Yuan, W., Zhou, H. Y., et al. 2010, *ApJL*, **716**, L31
- Alexander, T. 1997, in *Astrophysics and Space Science Library*, 218, *Astronomical Time Series*, ed. D. Maoz, A. Sternberg, & E. M. Leibowitz (Dordrecht: Kluwer), 163
- Bentz, M. C., Denney, K. D., Grier, C. J., et al. 2013, *ApJ*, **767**, 149
- Blandford, R. D., & McKee, C. F. 1982, *ApJ*, **255**, 419
- Boroson, T. A. 2002, *ApJ*, **565**, 78
- Capellupo, D. M., Netzer, H., Lira, P., Trakhtenbrot, B., & Mejía-Restrepo, J. 2015, *MNRAS*, **446**, 3427
- Chelouche, D., Pozo-Núñez, F., & Zucker, S. 2017, *ApJ*, **844**, 146
- Collin, S., Kawaguchi, T., Peterson, B. M., & Vestergaard, M. 2006, *A&A*, **456**, 75
- Czerny, B. 2019, *OAsT*, **28**, 200
- Czerny, B., & Hryniewicz, K. 2011, *A&A*, **525**, L8
- Czerny, B., Hryniewicz, K., Maity, I., et al. 2013, *A&A*, **556**, A97
- Czerny, B., Li, Y.-R., Hryniewicz, K., et al. 2017, *ApJ*, **846**, 154
- Czerny, B., Olejak, A., Rałowski, M., et al. 2019a, *ApJ*, **880**, 46
- Czerny, B., Schwarzenberg-Czerny, A., & Loska, Z. 1999, *MNRAS*, **303**, 148
- Czerny, B., Wang, J.-M., Du, P., et al. 2019b, *ApJ*, **870**, 84
- Dalla Bontà, E., Peterson, B. M., Bentz, M. C., et al. 2020, arXiv:2007.02963
- Denney, K. D., Pogge, R. W., Assef, R. J., et al. 2013, *ApJ*, **775**, 60
- Dong, X.-B., Wang, J.-G., Ho, L. C., et al. 2011, *ApJ*, **736**, 86
- Dong, X.-B., Wang, T.-G., Wang, J.-G., et al. 2009, *ApJL*, **703**, L1
- Du, P., Hu, C., Lu, K.-X., et al. 2014, *ApJ*, **782**, 45
- Du, P., Hu, C., Lu, K.-X., et al. 2015, *ApJ*, **806**, 22
- Du, P., Lu, K.-X., Zhang, Z.-X., et al. 2016, *ApJ*, **825**, 126
- Du, P., & Wang, J.-M. 2019, *ApJ*, **886**, 42
- Du, P., Zhang, Z.-X., Wang, K., et al. 2018, *ApJ*, **856**, 6
- Edelson, R. A., & Krolik, J. H. 1988, *ApJ*, **333**, 646
- Fonseca Alvarez, G., Trump, J. R., Homayouni, Y., et al. 2020, *ApJ*, **899**, 73
- Foreman-Mackey, D., Hogg, D. W., Lang, D., & Goodman, J. 2013, *PASP*, **125**, 306
- Gaskell, C. M. 2009, *NewAR*, **53**, 140
- Gaskell, C. M., & Peterson, B. M. 1987, *ApJS*, **65**, 1
- Gravity Collaboration, Sturm, E., Dexter, J., et al. 2018, *Natur*, **563**, 657
- Grier, C. J., Trump, J. R., Shen, Y., et al. 2017, *ApJ*, **851**, 21
- Haas, M., Chini, R., Ramolla, M., et al. 2011, *A&A*, **535**, A73
- Homayouni, Y., Trump, J. R., Grier, C. J., et al. 2020, *ApJ*, **901**, 55
- Hook, I. M., McMahon, R. G., Boyle, B. J., & Irwin, M. J. 1994, *MNRAS*, **268**, 305
- Hunter, J. D. 2007, *CSE*, **9**, 90
- Ichikawa, K., Packham, C., Ramos Almeida, C., et al. 2015, *ApJ*, **803**, 57
- Ivezić, Ž., Kahn, S. M., Tyson, J. A., et al. 2019, *ApJ*, **873**, 111
- Kaspi, S., Smith, P. S., Netzer, H., et al. 2000, *ApJ*, **533**, 631
- Kelly, B. C., Bechtold, J., & Siemiginowska, A. 2009, *ApJ*, **698**, 895

- Kovačević-Dojčinović, J., & Popović, L. Č. 2015, *ApJS*, **221**, 35
- Kozłowski, S. 2016, *ApJ*, **826**, 118
- Kozłowski, S., Kochanek, C. S., Udalski, A., et al. 2010, *ApJ*, **708**, 927
- Lawrence, A., & Elvis, M. 2010, *ApJ*, **714**, 561
- Li, I.-Hsiu, J., Shen, Y., Brandt, W. N., et al. 2019, *ApJ*, **884**, 119
- Lira, P., Kaspi, S., Netzer, H., et al. 2018, *ApJ*, **865**, 56
- Lusso, E., & Risaliti, G. 2017, *A&A*, **602**, A79
- MacLeod, C. L., Ivezić, Ž., Kochanek, C. S., et al. 2010, *ApJ*, **721**, 1014
- Martínez-Aldama, M. L., Czerny, B., Kawka, D., et al. 2019, *ApJ*, **883**, 170
- Marziani, P., & Sulentic, J. W. 2014, *MNRAS*, **442**, 1211
- Marziani, P., Zamanov, R. K., Sulentic, J. W., & Calvani, M. 2003, *MNRAS*, **345**, 1133
- McLure, R. J., & Jarvis, M. J. 2002, *MNRAS*, **337**, 109
- Mejía-Restrepo, J. E., Lira, P., Netzer, H., Trakhtenbrot, B., & Capellupo, D. M. 2018, *NatAs*, **2**, 63
- Metzroth, K. G., Onken, C. A., & Peterson, B. M. 2006, *ApJ*, **647**, 901
- Naddaf, M.-H., Czerny, B., & Szczerba, R. 2020, *FrASS*, **7**, 15
- Negrete, C. A., Dultzin, D., Marziani, P., et al. 2018, *A&A*, **620**, A118
- Netzer, H. 2013, *The Physics and Evolution of Active Galactic Nuclei* (1st edn; Cambridge: Cambridge Univ. Press)
- Netzer, H. 2020, *MNRAS*, **494**, 1611
- Oliphant, T. 2015, *NumPy: A Guide to NumPy* (2nd edn; USA: CreateSpace Independent Publishing Platform), <http://www.numpy.org/>
- Panda, S., Martínez-Aldama, M. L., & Zajaček, M. 2019a, *FrASS*, **6**, 75
- Panda, S., Marziani, P., & Czerny, B. 2019b, *ApJ*, **882**, 79
- Pedregosa, F., Varoquaux, G., Gramfort, A., et al. 2011, *Journal of Machine Learning Research*, **12**, 2825
- Peterson, B. M., Ferrarese, L., Gilbert, K. M., et al. 2004, *ApJ*, **613**, 682
- Peterson, B. M., & Horne, K. 2004, *AN*, **325**, 248
- Peterson, B. M., Wanders, I., Bertram, R., et al. 1998a, *ApJ*, **501**, 82
- Peterson, B. M., Wanders, I., Horne, K., et al. 1998b, *PASP*, **110**, 660
- Rakshit, S., Stalin, C. S., & Kotilainen, J. 2020, *ApJS*, **249**, 17
- Richards, G. T., Lacy, M., Storrie-Lombardi, L. J., et al. 2006, *ApJS*, **166**, 470
- Risaliti, G., & Lusso, E. 2019, *NatAs*, **3**, 272
- Rodríguez-Pascual, P. M., Alloin, D., Clavel, J., et al. 1997, *ApJS*, **110**, 9
- Sánchez-Sáez, P., Lira, P., Mejía-Restrepo, J., et al. 2018, *ApJ*, **864**, 87
- Seabold, S., & Perktold, J. 2010, in *Proc. 9th Python in Science Conference, Statsmodels: Econometric and Statistical Modeling with Python*, ed. S. van der Walt & W. J. Millman (Trieste: SISSA), 92
- Shakura, N. I., & Sunyaev, R. A. 1973, *A&A*, **500**, 33
- Shen, Y., Hall, P. B., Horne, K., et al. 2019, *ApJS*, **241**, 34
- Shen, Y., & Ho, L. C. 2014, *Natur*, **513**, 210
- Shen, Y., Horne, K., Grier, C. J., et al. 2016, *ApJ*, **818**, 30
- Shen, Y., Richards, G. T., Strauss, M. A., et al. 2011, *ApJS*, **194**, 45
- Śniegowska, M., Kozłowski, S., Czerny, B., & Panda, S. 2020, *ApJ*, **900**, 64
- Taylor, M. B. 2005, in *ASP Conf. Ser. 347, adass XIV*, ed. P. Shopbell, M. Britton, & R. Ebert (San Francisco, CA: ASP), 29
- Trakhtenbrot, B., & Netzer, H. 2012, *MNRAS*, **427**, 3081
- Vestergaard, M., & Osmer, P. S. 2009, *ApJ*, **699**, 800
- Vestergaard, M., & Peterson, B. M. 2006, *ApJ*, **641**, 689
- Vestergaard, M., & Wilkes, B. J. 2001, *ApJS*, **134**, 1
- Wang, J.-M., Du, P., Hu, C., et al. 2014a, *ApJ*, **793**, 108
- Wang, J.-M., Du, P., Li, Y.-R., et al. 2014b, *ApJL*, **792**, L13
- Wang, J.-M., Qiu, J., Du, P., & Ho, L. C. 2014c, *ApJ*, **797**, 65
- Watson, D., Denney, K. D., Vestergaard, M., & Davis, T. M. 2011, *ApJL*, **740**, L49
- Wilhite, B. C., Brunner, R. J., Grier, C. J., Schneider, D. P., & Vanden Berk, D. E. 2008, *MNRAS*, **383**, 1232
- Wilhite, B. C., VandenBerk, D. E., Kron, R. G., et al. 2005, *ApJ*, **633**, 638
- Yu, L.-M., Bian, W.-H., Zhang, X.-G., et al. 2020a, *ApJ*, **901**, 133
- Yu, L.-M., Zhao, B.-X., Bian, W.-H., Wang, C., & Ge, X. 2020b, *MNRAS*, **491**, 5881
- Yu, Z., Kochanek, C. S., Peterson, B. M., et al. 2020, *MNRAS*, **491**, 6045
- Zajaček, M., Czerny, B., Martínez-Aldama, M. L., et al. 2020, *ApJ*, **896**, 146
- Zajaček, M., Czerny, B., Martínez-Aldama, M. L., & Karas, V. 2019, *AN*, **340**, 577
- Zu, Y., Kochanek, C. S., Kozłowski, S., & Peterson, B. M. 2016, *ApJ*, **819**, 122
- Zu, Y., Kochanek, C. S., Kozłowski, S., & Udalski, A. 2013, *ApJ*, **765**, 106
- Zu, Y., Kochanek, C. S., & Peterson, B. M. 2011, *ApJ*, **735**, 80